Photonuclear and radiative-capture reaction rates for nuclear astrophysics and transmutation: $^{92-100}$Mo, ^{88}Sr, ^{90}Zr, and ^{139}La

M. Beard,[1,2,*] S. Frauendorf,[1,2,†] B. Kämpfer,[1,3,‡] R. Schwengner,[1,§] and M. Wiescher[2,‖]
[1]*Institut für Strahlenphysik, Helmholtz-Zentrum Dresden-Rossendorf, D-01314 Dresden, Germany*
[2]*Department of Physics, University of Notre Dame, Notre Dame, Indiana 46556, USA*
[3]*Institut für Theoretische Physik, Technische Universität Dresden, D-01062 Dresden, Germany*
(Received 13 May 2011; revised manuscript received 17 April 2012; published 22 June 2012)

Experimental photoabsorption cross sections for the nuclei ^{92,94,96,98,100}Mo, ^{88}Sr, ^{90}Zr, and ^{139}La are used as an input for calculations of (γ, n), (γ, p), and (γ, α), as well as (n, γ), (p, γ), and (α, γ) cross sections and reaction rates at energies and temperatures relevant for nucleosynthesis network models and transmutation projects. The calculations are performed with the statistical-model code TALYS. The results are compared with those obtained by using different analytic standard parametrizations of γ-ray strength functions implemented in TALYS and with an energy-damped double-Lorentzian model. The radiative capture reaction cross sections are enhanced by the pygmy resonances in ^{88}Sr, ^{90}Zr, and ^{139}La.

DOI: 10.1103/PhysRevC.85.065808 PACS number(s): 25.20.Lj, 25.40.Lw, 27.60.+j, 28.65.+a

I. INTRODUCTION

The vast majority of nuclei heavier than iron are synthesized via either the slow (s) or rapid (r) process of neutron capture. There are however 35 naturally occurring nuclei located on the neutron-deficient side of the valley of stability, including the nuclei ^{92}Mo, ^{94}Mo, and ^{138}La [1]. This location excludes the possibility of a production through neutron capture mechanisms. It has been proposed that these nuclei, known as p nuclei, are formed via the p process. The nature of the p process is not yet fully understood, nor is the actual site for the p process clearly identified [1]. The presently favored scenario describes the p process primarily as a sequential photodissociation process of stable nuclei, which occurs when the expanding shock front of a core collapse supernova transverses the neon oxygen shell burning regions of the presupernova star [2]. The pre existing s process abundance distribution in these layers is shifted by (γ, n) processes to the neutron deficient side. With increasing neutron threshold (γ, n) reactions become less likely and the reaction flow is dominated by (γ, α) reactions, shifting the abundance distribution towards lower masses while liberating α particles. It has been demonstrated that for closed shell nuclei the (γ, α) flux is replaced by a (γ, p) dominated reaction flow towards the line of stability, since the α threshold at closed shell even-even nuclei becomes so large that the proton decay emerges as the favored mechanism [3]. Figure 1 shows the typical reaction path for the p process as calculated in the framework of a parameterized shock expansion model [3]. In the mass range below the $N = 50$ closed shell nuclei the photodissociation flux pattern is supplemented with neutron and charged particle induced reactions and β^+ decay, as can be clearly seen in the figure. Analysis of meteoric samples provide quantitative data for the abundance of p process nuclei. Such abundance observations exhibit within a factor of 3 agreement with the predictions from model simulations, such as described above, except for the very light p nuclei ^{92}Mo, ^{94}Mo, and ^{138}La (amongst others), which are found to be significantly overabundant compared to model predictions [1].

Modeling p nuclei abundances (as well as all other isotopic abundances resulting from nucleosynthesis processes) requires the detailed knowledge of thousands of nuclear reactions associated with the p process path. Since experimental data regarding pertinent nuclear reactions in energy regions of relevance to nuclear astrophysics is limited, data must often be obtained from global parameters. While there have been a number of experimental studies with photon beams at facilities such as the Dalinac at the TU Darmstadt [4] or the ELBE accelerator at the Helmholtz-Zentrum Dresden-Rossendorf (HZDR) [5], most of the experimental data rely on inverse radiative capture studies at energies between 3 MeV and 12 MeV, which were performed at ATOMKI, Debrecen Hungary, PTB Braunschweig Germany, Demokritos Lab, Athens Greece, and the NSL at the University of Notre Dame, USA (e.g., [6,7]). These studies have the advantage that all reaction and decay channels in the compound region of the excited nucleus can be studied in comparison to Hauser Feshbach (HF) statistical model simulations. This is critical since most of the p process model simulations rely on reaction rates derived from the statistical model approach. These studies indicated systematic deviations in the quality of the HF predictions, which point to systematic deviations associated with the γ channel.

There are many necessary ingredients for a HF calculation, including knowledge of the nuclear level densities, particle optical potentials and γ-ray strength functions, which characterize the emission and absorption of photons. Because network calculations, performed to simulate astrophysical processes, require a large reaction database, the use of global descriptions for quantities such as level density and giant dipole resonance (GDR) parameters is paramount. Since the p process is largely a photodissociation mechanism, detailed

*mbeard@nd.edu
†stefan.g.frauendorf.1@nd.edu
‡kaempfer@hzdr.de
§r.schwengner@hzdr.de
‖michael.c.wiescher.1@nd.edu

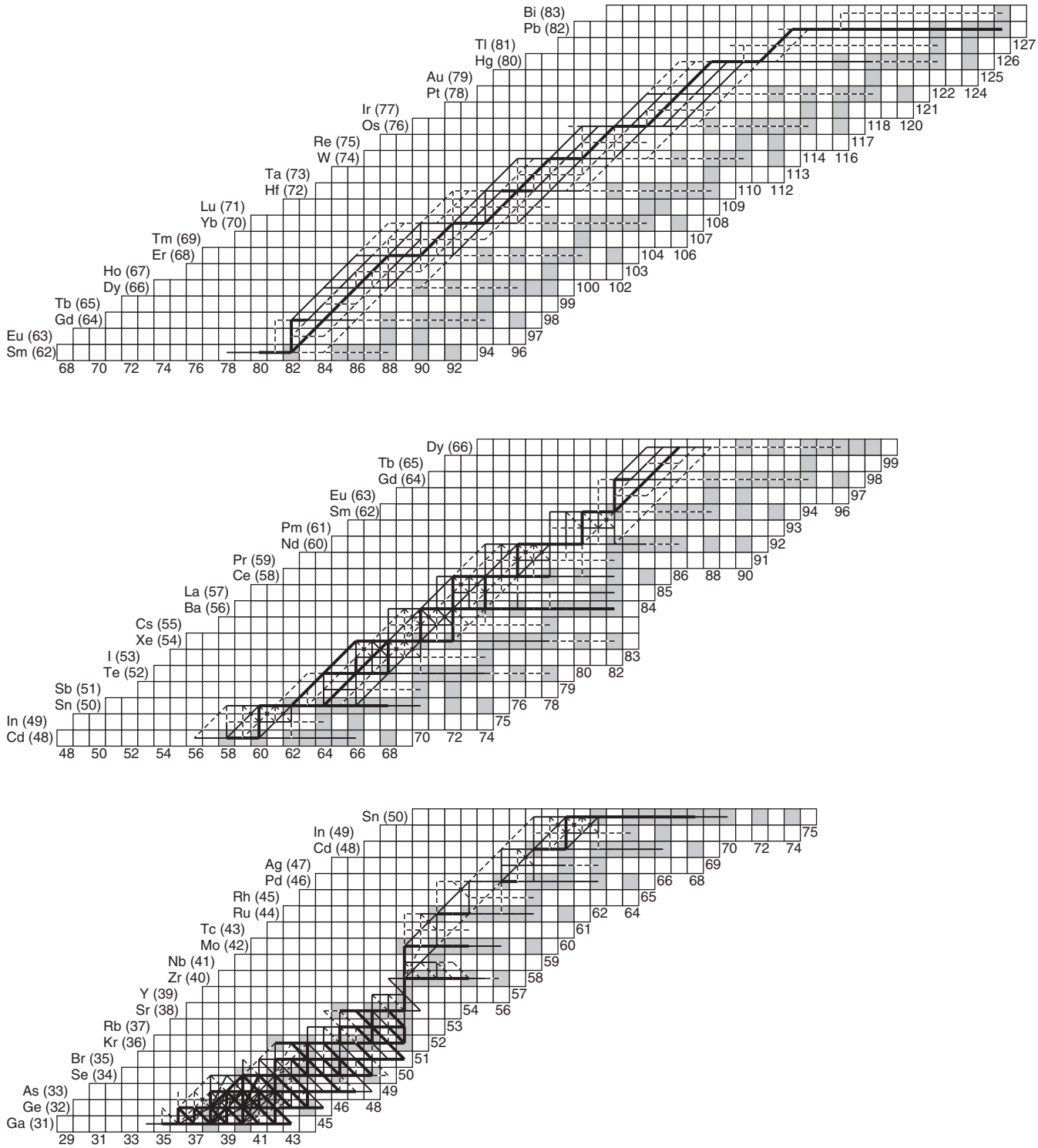

FIG. 1. Typical reaction path for the p process during the first second of a shock expansion front passing through the O/Ne layers. Taken from Rapp *et al*. [3].

knowledge of the γ-ray strength function, or the related quantity the photoabsorption cross section, is also crucial, especially in the region of the neutron threshold. Presently employed HF predictions have been obtained by describing the photoabsorption cross section as either a single or two Lorentzian curves (to account for nuclear deformation), which are then smoothly extrapolated to below the neutron threshold. An approach such as this however may miss extra strength caused by a resonance structure near the neutron threshold, as, e.g., reported in Ref. [8].

An improved knowledge of photoabsorption cross sections is also required for future nuclear technologies. The measurement and modeling of neutron capture and inelastic neutron scattering cross sections is currently one of the primary ways to study suitable reactions for transmutating long-lived nuclides, produced in nuclear-fuel cycles, into short-lived nuclides. In this context, new facilities at neutron sources have been developed, such as the γ-calorimeter DANCE at the Los Alamos Neutron Science Center [9], n_TOF at CERN [10], GELINA at IRMM [11], and nELBE at HZDR [12]. The reactions of interest populate excited states in an energy range of high level density. The de-excitation of states by γ-ray emission is considered to be statistical. It is determined by the level density as a function of excitation energy and by γ-ray strength functions, or the related photoabsorption cross sections. The precise knowledge of these quantities is therefore a necessary ingredient for the reliable determination of reaction cross sections via the measurement of γ rays. In this context it is hoped that improved nuclear cross section estimates, based on realistic γ-ray strength functions, can be translated into new developments for nuclear waste transmutation programs.

Recently, new (γ, γ') cross section measurements were performed using the bremsstrahlung facility at ELBE [13] for the nuclei ^{92,94,96,98,100}Mo [14,15], ^{88}Sr [16], ^{90}Zr [17], and ^{139}La [18]. The measurements probed the photoabsorption cross section from an energy of approximately 4.5–6 MeV up to the neutron threshold. It is the aim of the present paper to use the HF model to calculate photoinduced and radiative capture reactions using these new γ-ray strength function data. Cross sections and reaction rates currently used for astrophysical and transmutation purposes, from for instance the RIPL-2 [19] database, rely on phenomenological Lorentzian extrapolations. The purpose of this study is twofold, firstly to analyze the effect of using experimental strength functions (in opposed to extrapolations), and secondly to evaluate the impact of the pygmy resonances on cross section and reaction rate calculations. This will provide an opportunity to test the accuracy of the existing strength function models.

Our paper is organized as follows. In Sec. II we describe the method for calculating the reaction cross sections of interest, with particular emphasis on existing photoabsorption models and the implementation of the experimental photoabsorption cross section data. For selected nuclei only, the results of the calculated reaction cross sections and reaction rates are presented in Secs. III and IV, respectively. (See supplemental material for additional cross section and reaction rate results, which also contains comparisons with the popular NON-SMOKER reaction rates [20].) A detailed discussion of the results is provided in Sec. V. Finally, we conclude in Sec. VI.

II. CROSS SECTION CALCULATIONS

A. Statistical model

Calculations were performed using the computer code TALYS [21], which is a standard nuclear reaction code that can calculate reaction cross sections with the statistical HF model [22]. Statistical reaction theory is based on the concept of the compound nucleus, which decays according to the laws of statistics after having lost almost all information about its formation. The only exceptions are the energy, the angular momentum, and the parity, which are strictly conserved. For a given combination of the conserved quantities, the probability of a specific reaction is the product of the probability for formation of the compound nucleus in the entrance channel and the probability for its decay into the exit channel. The respective probabilities are expressed in terms of the transmission coefficients $T_j(E, J, \pi; E_i^\mu, J_i^\mu, \pi_i^\mu; E_j, J_j, \pi_j; e_{ij})$, where E, J, π denote the excitation energy, angular momentum, and parity of the compound nucleus. Here, j denotes the emitted particle with excitation energy, angular momentum, and parity given by E_j, J_j, and π_j respectively. Only for composite ejectiles, like the α particle, does one need E_j; it is assumed that it remains in its ground state. The residual nucleus is represented by i, with excitation energy, angular momentum, and parity given by E_i^μ, J_i^μ, and π_j^μ. Excited states are denoted by μ. The kinetic energy of the emitted particle is e_{ij}. Energy conservation implies $E = E_i^\mu + E_j + e_{ij}$, where the ground state energies are assumed to be included. Conservation of angular momentum involves several combinations of J_i^μ, J_j, and l coupling to J, where l is the angular momentum of the partial wave. Accordingly, the transmission coefficient is a sum of terms that correspond to the various couplings of the angular momenta. Only terms that obey conservation of parity [i.e., $\pi = \pi_i^\mu \pi_j (-1)^l$] are allowed. The same holds for the inverse absorption reaction. In this case i labels the target nucleus and μ its excited states. In the astrophysical context, one is mainly interested in the total cross section for reactions $i(j, o)m$, where projectile j hits nucleus i, and ejectile o is emitted leaving residual nucleus m. Usually one is not interested in the specific excitation energy, parity, or angular momentum of either the ejectile or the residue. Hence, all exit channels that comply with the conservation laws contribute to the formation of the ejectile and the residual nucleus. The corresponding cross section for absorbing the particle j by the nucleus i in excited state μ, emitting particle m and leaving residue o is

$$\sigma[i^\mu(j,o)m, e_{ij}] = \frac{\pi}{k_{ij}^2 \left(2J_i^\mu + 1\right)(2J_j + 1)} \times \sum_{J,\pi} (2J+1) \frac{T_j\left(E, J, \pi; E_i^\mu, J_i^\mu, \pi_i^\mu; E_j, J_j, \pi_j; e_{ij}\right) T_o(E, J, \pi; E_o, J_o, \pi_o)}{T_{\text{tot}}(E, J, \pi)}, \quad (1)$$

$$T_o(E, J, \pi; E_o, J_o, \pi_o) = \sum_\nu T_o\left(E, J, \pi; E_m^\nu, J_m^\nu, \pi_m^\nu; E_o, J_o, \pi_o; e_{mo}\right). \quad (2)$$

The wave number of the projectile is given by k_{ij}. For photo reactions ($j = \gamma$), k_{ij} coincides with the wave number of the photon. In the case of a massive projectile, $k_{ij} = \sqrt{2\mu_{ij}e_{ij}}/\hbar^2$ where μ_{ij} is the reduced mass of projectile and target. The sum ν runs over all excited states of the residue. The cross section (1) has the simple structure of the statistical reaction model. The first line is the probability for compound nucleus formation. The second line is the probability for compound nucleus decay into the exit channel of interest. It is the ratio of the transmission coefficient for this channel divided by the total transmission coefficient $T_{\rm tot}(E, J, \pi)$, which is the sum of the transmission coefficients of all channels into which the compound nucleus can decay.

Laboratory experiments measure the cross section of the projectile hitting the target in the ground state $\mu = 0$ (i.e., $\sigma[i^0(j, o)m, e_{ij}]$). In the stellar environment the reactions take place in a hot plasma, where excited target states are thermally populated. The cross section for this is given by

$$\sigma^*[i(j, o)m, e_{ij}] = \frac{1}{\sum_\mu \left(2J_I^\mu + 1\right)\exp\left(-E_i^\mu/kT\right)} \times \sum_\mu \left\{\left(2J_I^\mu + 1\right)\exp\left(-E_i^\mu/kT\right)\sigma[i^\mu(j, o)m, e_{ij}]\right\}. \quad (3)$$

The stellar reaction rate $\langle\sigma v\rangle$ in the plasma is given by folding the cross section with the thermal flux of projectiles impinging the target, which, for massive particles, is

$$\langle\sigma v\rangle = \frac{\frac{2}{\mu_{ij}}\int_0^\infty e_{ij}\sigma^*[i(j, o)m, e_{ij}]\exp(-e_{ij}/kT)de_{ij}}{\int_0^\infty e_{ij}^{1/2}\exp(-e_{ij}/kT)de_{ij}}. \quad (4)$$

In the case of photoreactions it is

$$\langle\sigma v\rangle = \frac{c\int_0^\infty e_\gamma^{1/2}\sigma^*[i(\gamma, o)m, e_\gamma]\exp(-e_\gamma/kT)de_\gamma}{\int_0^\infty e_\gamma^{1/2}\exp(-e_\gamma/kT)de_\gamma}. \quad (5)$$

The transmission coefficients for the particle channels are obtained from the S matrix for elastic scattering, which is calculated for an appropriate optical model potential. The choice of the optical potential is one source of uncertainty. An additional source of uncertainty comes from the level density, which is introduced because the summation in Eq. (2) over the final states of the residue typically involves a huge number of terms. In order to carry out the sum, above some excitation energy $E_m^{\rm max}$ one replaces it with an integral over the level density $\rho(E_m, J_m, \pi_m)$

$$T_o(E, J, \pi; E_o, J_o, \pi_o) = \sum_\nu^{E_m^\nu < E_m^{\rm max}} T_o^\nu\left(E, J, \pi; E_m^\nu, J_m^\nu, \pi_m^\nu; E_o, J_o, \pi_o; e_{mo}\right) + \sum_{J_m,\pi_m}\int_{E_m^{\rm max}}^{E-E_m^0} T_o(E, J, \pi; E_m, J_m, \pi_m; E_o, J_o, \pi_o; e_{mo}) \times \rho(E_m, J_m, \pi_m)dE_m. \quad (6)$$

Addressing the uncertainties arising from the optical potential and level density models is beyond the scope of this paper, which is primarily focused on the uncertainties associated with the γ-transmission coefficients.

B. γ-strength models

The angular momentum of the photon is given by its multipolarity J_γ. Here we consider only the dipole radiation since higher multipoles play an insignificant role for thermonuclear rates in astrophysics. Electric dipole radiation (E1) dominates. The E1 photon has negative parity. Its transmission coefficient is expressed in terms of the strength function $f_{\rm E1}(E_\gamma)$,

$$T_\gamma(E, 1, -; E_\gamma, 1, -) \equiv T_{\rm E1}(E_\gamma) = 2\pi f_{\rm E1}(E_\gamma)E_\gamma^3. \quad (7)$$

The magnetic dipole radiation (M1) is usually much weaker. The M1 photon and has positive parity. In terms of the strength function $f_{\rm M1}(E_\gamma)$, the M1 transmission coefficient is given by

$$T_\gamma(E, 1, +; E_\gamma, 1, +) \equiv T_{\rm M1}(E_\gamma) = 2\pi f_{\rm M1}(E_\gamma)E_\gamma^3. \quad (8)$$

Because there is a limited amount of experimental data available for the M1 GDR, there are no systematic parameters to describe it, unlike the situation for E1. For our calculations we have made use of the option in TALYS to describe the M1 resonance in terms of Eq. (10), discussed below.

The cross section for dipole radiation absorption is

$$\sigma_\gamma(E_\gamma) = 3(\pi\hbar c)^2 E_\gamma[f_{\rm E1}(E_\gamma) + f_{\rm M1}(E_\gamma)], \quad (9)$$

where E_γ is the incident γ-ray energy. It is the sum of the E1 and M1 γ-ray strength functions and transmission functions that are obtained from experimental photoabsorption cross section data. Only the measurement of the absorption of polarized gamma radiation can provide the individual E1 and M1 components.

The right side of expression (7) is assumed to depend only on E_γ, whereas the left depends on E as well. This is the Brink-Axel hypothesis, which assumes that the ground state GDR can be built on each excited state. Traditionally, the E1 strength functions have been described by the single Lorentzian (SLO) form of Brink-Axel [23],

$$f_{\rm E1}(E_\gamma) = \frac{\sigma_{\rm GDR}\Gamma_{\rm GDR}}{3(\pi\hbar c)^2}\frac{E_\gamma\Gamma_{\rm GDR}}{\left(E_\gamma^2 - E_{\rm GDR}^2\right)^2 + E_\gamma^2\Gamma_{\rm GDR}^2}, \quad (10)$$

where $\Gamma_{\rm GDR}$ is the width and $E_{\rm GDR}$ the energy of the giant dipole resonance (GDR), and $\sigma_{\rm GDR}$ stands for the cross section at $E_{\rm GDR}$. The E1 GDR parameters are obtained from the RIPL-2 database [19]. In the case of M1, $E_{\rm M1,GDR} = 41A^{-1/3}$ and $\Gamma_{\rm M1,GDR} = 4$ MeV. By evaluating the function $f_{\rm M1,GDR} = 1.58A^{0.47}$, one obtains the M1 strength function at 7 MeV. Applying Eq. (10) at 7 MeV yields $\sigma_{\rm M1,GDR}$, and so the M1 GDR can be fully described at all energies by Eq. (10).

A second description of the E1 GDR is the generalized Lorentzian (GLO) form of Kopecky-Uhl [24]. This approach takes the excitation energy E of the compound nucleus into

account,

$$f_{\mathrm{E1}}(E_\gamma) = \frac{\sigma_{\mathrm{GDR}}\Gamma_{\mathrm{GDR}}}{3(\pi\hbar c)^2}\left(\frac{E_\gamma\Gamma(E_\gamma)}{\left(E_\gamma^2 - E_{\mathrm{GDR}}^2\right)^2 + E_\gamma^2\Gamma(E_\gamma)^2} + \frac{0.7\Gamma_{\mathrm{GDR}}4\pi^2T^2}{E_{\mathrm{GDR}}^5}\right),$$
$$\Gamma(E_\gamma) = \Gamma_{\mathrm{GDR}}\frac{E_\gamma^2 + 4\pi^2T^2}{E_{\mathrm{GDR}}^2}. \tag{11}$$

The quantity T in Eq. (11) is the nuclear temperature at the final state reached after emission or absorption of the photon. If the back-shifted Fermi gas model (BSFG) is used it is given by Ref. [24]

$$T = \sqrt{\frac{E-\Delta}{a}}, \tag{12}$$

where E is the energy of the final state, a is the Fermi gas level density parameter, and Δ is the pairing correction. The GLO was devised for (n,γ) reactions with thermal neutron capture. In this case $E = E_n + S_n - E_\gamma$ where S_n represents the neutron separation energy and E_n is the neutron incident energy.

The SLO and GLO models do not explicitly take into account the splitting of the GDR by deformation. Triaxial deformation is built into the treatment of Ref. [25]. According to this model the E1 strength function is parametrized as a sum of three Lorentz curves, of spreading width Γ_k, each corresponding to a nuclear E1 dipole vibration along one of the three principal axes. The resonance energies and widths of the nuclear GDR are characterized in terms of the deformation parameters β and γ. The GDR centroid energies are obtained from symmetry energy and surface stiffness, which in turn have been determined from a fit to finite range droplet model nuclear masses [26] with $R = r_0A^{1/3}$, $r_0 = 1.16$ fm, $J = 32.7$ MeV, and $Q = 29.2$ MeV. Within this framework the E1 strength function is given by

$$f_{\mathrm{E1}}(E_\gamma) = \frac{\sigma_{\mathrm{GDR}}\Gamma_{\mathrm{GDR}}}{3(\pi\hbar c)^2}\frac{1.02}{3}\sum_{k=1}^{3}\frac{E_\gamma\Gamma_k(E_k)}{\left(E_k^2 - E_\gamma^2\right)^2 + E_\gamma^2\Gamma_k(E_k)^2},$$
$$\Gamma_k(E_k) = 1.99\ \mathrm{MeV}\left(\frac{E_k}{10\,\mathrm{MeV}}\right)^{\delta},$$
$$E_k = \frac{E_G}{\exp\left(\sqrt{5/4\pi}\,\beta\cos\left(\gamma - \frac{2}{3}k\pi\right)\right)},$$
$$E_G = \hbar c\left[\frac{8Jt}{R^2m^*}\left(1 + u - \frac{1+\psi+3u}{1+\psi+u}\right)^{-1}\right]^{1/2}, \tag{13}$$

where the values of δ and ψ are 1.6 and 0.0768 respectively, and $t = A^2/(4NZ)$, while $u = (1-\psi)\mu$ and $\mu = 3Jr_0/(QR)$. The effective mass $m^* = 0.7m$, where m refers to the mass of the proton. The parameters σ_{GDR} and Γ_{GDR} are the cross section and width of a spherical nucleus with the same mass. We refer to this E1 strength function model as the triple Lorentzian (TLO).

In addition to these three E1 strength function models, there is also the model of Ref. [27], which assumes axial symmetry. We refer to this model as the double Lorentzian (DLO), and note that it is used in the HF computer code NON-SMOKER [28]. The GDR is composed of two Lorentzian dipole vibrations $(k = 1, 2)$ along, and perpendicular to, the axis of rotational symmetry. Taking into account the neutron-proton exchange term $\chi = 0.2$ [29], $f_{\mathrm{E1}}(E_\gamma)$ is given by

$$f_{\mathrm{E1}}(E_\gamma) = \frac{\sigma_{\mathrm{GDR}}\Gamma_{\mathrm{GDR}}}{3(\pi\hbar c)^2}\frac{1.2}{3}\sum_{k=1}^{2}k \times \frac{E_\gamma\Gamma_{G,k}(E_{G,k})}{\left(E_\gamma^2 - E_{G,k}^2\right)^2 + E_\gamma^2\Gamma_{G,k}(E_{G,k})^2},$$
$$\Gamma_{G,k}(E_{G,k}) = \sqrt{\frac{E_\gamma}{E_{G,k}}}(0.185E_{G,k} + 0.57k|G_{k-1}|E_{G,k}\xi_2),$$
$$E_{G,1} + 2E_{G,2} = 3E_G, \quad E_{G,2}/E_{G,1} = 0.911\eta + 0.089, \tag{14}$$

where E_G is given by Eq. (13), which was suggested by Ref. [30]. Equation (14) is appropriate for deformed nuclei. The static deformation parameter β_0 has been obtained from the hydrodynamic droplet model of Ref. [31], which includes shell structure and is based on the shell correction term. The quantity ξ_2 is the root-mean-square value of $\xi = \beta - \beta_0$, which is the deviation of the deformation parameter β from its static value. The parameter $\eta(\beta_0)$ is the ratio of the diameter of the nuclear symmetry axis to the perpendicular diameter as given by the hydrodynamic model, while G_0 and G_1 are given respectively by

$$G_0 = \frac{D}{\beta_0}\left(\frac{-1}{1+D} + \frac{0.08}{1+0.08D}\right),$$
$$G_1 = \frac{-D}{\beta_0}\left(\frac{-1}{1-D} + \frac{0.08}{1-0.08D}\right), \tag{15}$$

and D is a dimensionless parameter containing the static deformation, equal to $D = (4\pi/5)^{-1/2}\beta_0$. For deformed nuclei, E_G is interpreted as the average peak energy of the two Lorentzians and is found from Eq. (13) using the parameters $t = 1$, $u = \mu$, $r_0 = 1.18$, $J = 36.8$ MeV, and $Q = 17$ MeV. In the event that the nucleus is spherical, the sum over k in Eq. (14) disappears yielding $E_{G,k} = E_G$ and $\Gamma_{G,k} = \Gamma_G$. The width in this case is given by

$$\Gamma_G(E_G) = \alpha E_G^{\delta} + 2.35\sqrt{\frac{5}{8\pi}}E_G\beta_2, \tag{16}$$

in which β_2 is the root mean square of β. The dimensionless parameters α and δ are obtained from least-square fits to experimental GDR widths for nuclei where not only the widths, but also E_G and β_2 are all experimentally known. The root-mean-square values β_2 and ξ_2 are calculated for a harmonic oscillator with the stiffness C_2 and mass coefficient D_2, which are given by

$$C_2 = -\left.\frac{\partial^2B}{\partial\beta^2}\right|_{\beta_0}, \quad D_2 = D_{2\mathrm{irrot}}e^{(2.24-0.195E_{\mathrm{shell}})},$$
$$D_{2\mathrm{irrot}} = \frac{3AmR^2}{8\pi}, \tag{17}$$

where B is the binding energy and E_{shell} the shell correction energy as calculated in the hydrodynamic droplet model of Ref. [31].

C. Experimental photoabsorption cross section

Experimental (γ, γ') cross sections were taken over an energy range of $E^{\min}_{(\gamma,\gamma')} = 4.5$–6 MeV up to the neutron separation energy, $E^{\max}_{(\gamma,\gamma')} = S_n$ [14–18]. For the nuclei $^{94-100}$Mo photon-scattering data below 4 MeV also exists [32–36]. However, the extraction of a continuous strength function from these data is problematic because only a few discrete transitions exist. Therefore, we apply the approach described below. Radiative strength functions in the γ-ray energy range up to about 8 MeV have also been derived from measuring particle-γ coincidences following inelastic scattering of ^{3}He from even-mass Mo targets and following $(^3\text{He},\alpha\gamma)$ reactions on odd-mass Mo isotopes [37], which are at variance to the (γ, γ') results of Refs. [14,15]. In contrast to the direct measurement of the γ-absorption cross section in Refs. [14,15], however, the strength functions of Ref. [37] are derived in an indirect way. These reactions do not deliver an absolute scale for the electromagnetic strength, therefore the required information is taken from (n, γ) data. Studying the (n, γ) reaction on ^{96}Mo, Ref. [38] came to the conclusion that the data of Ref. [37] can be well accounted for with the GLO strength function model (except for the apparent up-bend at low energy, which according to Ref. [39] is not of large importance for the nuclei considered here).

The selection of the nuclei for the present study was motivated by the strong pygmy dipole strength in ^{88}Sr, ^{90}Zr, and ^{139}La, and the particular astrophysical relevance of the p process nuclei ^{92,94}Mo, as outlined in the Introduction. In addition, the Mo chain constitutes a sequence of isotopes ranging from spherical to deformed shapes. The (γ, γ') absorption cross sections from Refs. [14–18] cover an energy region $E^{\min}_{(\gamma,\gamma')} < E_\gamma \lesssim S_n$, with $E^{\min}_{(\gamma,\gamma')} = 4$ MeV. They smoothly connect with the absorption cross sections from Ref. [40], which allows us to derive the experimental dipole strength functions shown in Figs. 2 and 3. Below $E^{\min}_{(\gamma,\gamma')}$ there are data on transitions to discrete levels, which are also included in Figs. 2 and 3. However, we consider these values as irrelevant for the following reason: In the energy range $0 < E_\gamma < E^{\min}_{(\gamma,\gamma')}$ the strength function is only used to calculate the γ emission after particle capture. It describes transitions between dense compound levels and is expected to vary smoothly as a function of energy. The photoabsorption, on the other hand, reaches few discrete levels, which only appear above about 2 MeV. Obviously, the transition strength to these discrete levels must be different from the average transition strength

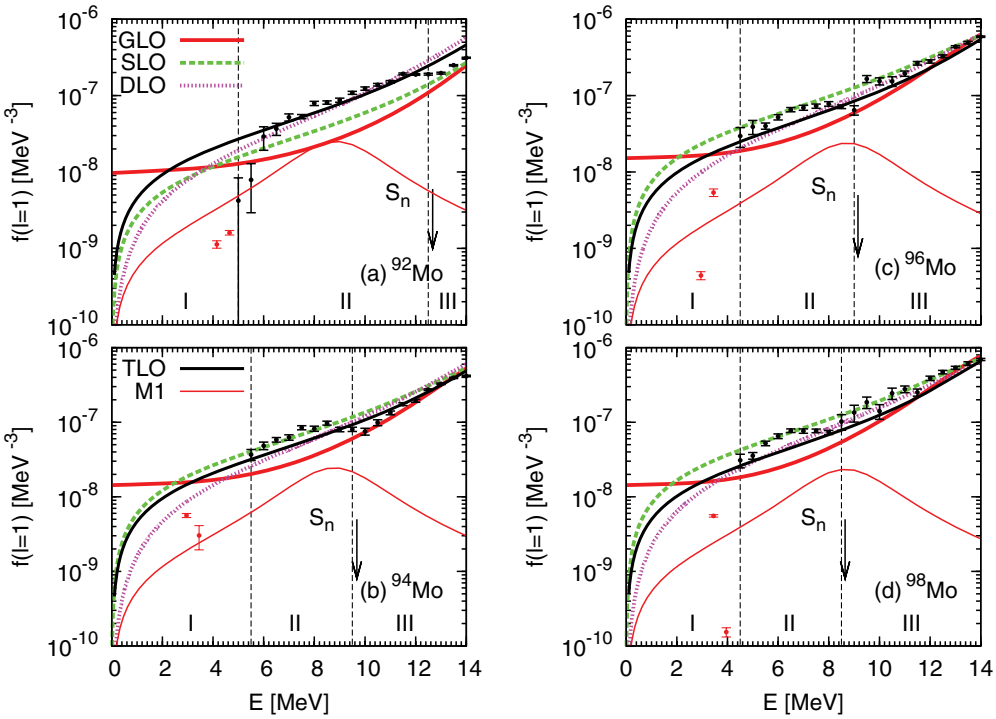

FIG. 2. (Color online) $l = 1$ strength functions for ^{92,94,96,98}Mo (a)–(d) as a function of energy $E \equiv E_\gamma$. Thick red curves refer to strength functions calculated using the GLO model, green dotted curves to strength functions from the SLO model and pink dotted curves are from NON-SMOKER, calculated with the DLO. The black points are experimental data, with error bars shown. Solid black curves refer to the TLO calculations, and provide an estimate of the strength function in the energy region of 0 to 4.5 MeV. Thin red curves represent the $M1$ strength function. Red points illustrate the strength function for discrete states in the compound nucleus. For $E < 4$ MeV, in panels (a) and (d) the red points are from Ref. [36], in panel (b) they are from Ref. [33] and in panel (c) they are from Ref. [34]. Where applicable, above 4 MeV red points are from Ref. [14]. The ones in panel (d) are additionally from Ref. [15]. For $4.5 \lesssim E \lesssim S_n$ black data points are from Refs. [14] [in panels (a)–(c)] and [15] [in panel (d)]. For all panels, black data points in the region $S_n \lesssim E$ are from Ref. [40] with corrections described in the text. The arrows depict the neutron separation energies S_n.

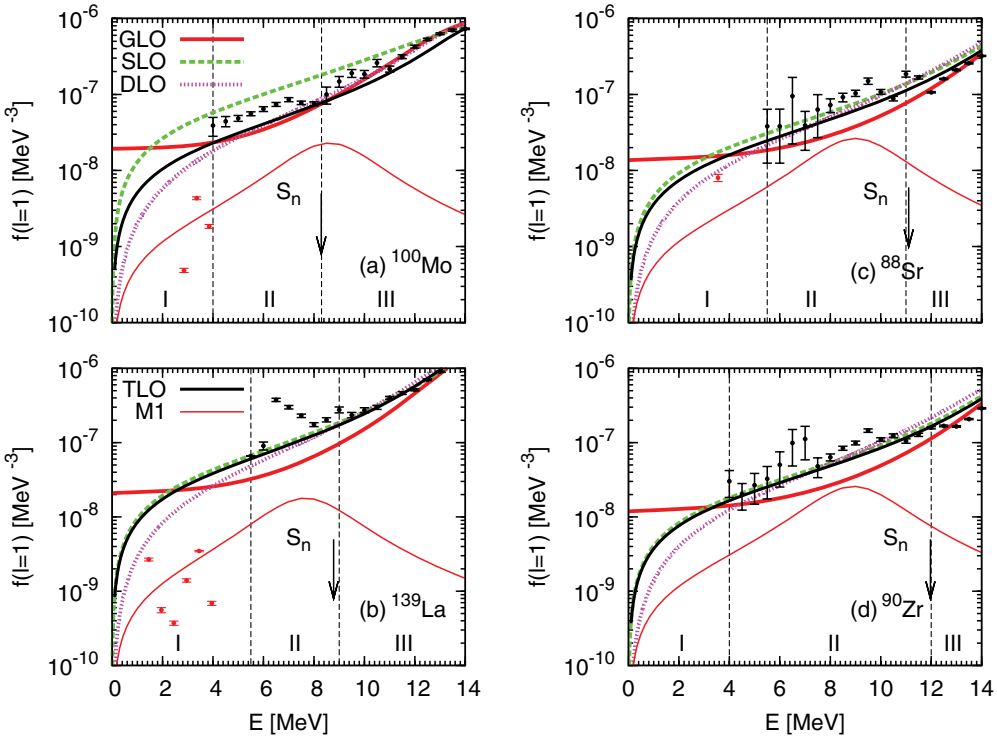

FIG. 3. (Color online) Same as Fig. 2, but for ^{100}Mo (a) ($4 \lesssim E \lesssim S_n$ data from [15]), ^{139}La (b) ($5.5 \lesssim E \lesssim S_n$ data from Ref. [18]), ^{88}Sr (c) ($6 \lesssim E \lesssim S_n$ data from Ref. [16]), and ^{90}Zr (d) ($4 \lesssim E \lesssim S_n$ data from Ref. [17]). Red data points are from Ref. [36] in panel (a), from Ref. [65] in panel (b), and from Ref. [66] in panel (c).

between compound levels. Therefore we have to use a model to describe the strength function for $E_\gamma < E^{\min}_{(\gamma,\gamma')}$. We have chosen to use the TLO, which reproduces the experimental strength functions reasonably well for $E_\gamma > E_{\min}$ (cf. Figs. 2 and 3).

In summary input photoabsorption cross sections for each nucleus were produced in the following manner.

(i) For the Mo isotopes in the low-energy region $0 \leqslant E_\gamma \leqslant E^{\min}_{(\gamma,\gamma')}$ the strength function was estimated according to the TLO parametrization proposed in Ref. [25] and set out in Eq. (13). Deformation parameters were taken from Ref. [36]. For the nuclei ^{88}Sr, ^{90}Zr, and ^{139}La, zero deformation was assumed. As such, the TLO low-energy strength function for these isotopes coincides with a single Lorentzian.

(ii) In the energy region $E^{\min}_{(\gamma,\gamma')} \leqslant E_\gamma \leqslant S_n$, the (γ,γ') experimental data were taken from Refs. [14–18].

(iii) For the region $S_n < E_\gamma < E_{\mathrm{GDR}} + \Delta$ (where $\Delta = 8$ MeV has been arbitrarily selected), (γ, n) data for ^{88}Sr, ^{90}Zr, $^{92-100}$Mo, and ^{139}La were taken from Refs. [41–44], respectively. These data are tabulated in the EXFOR data base [40]. Later measurements [45] suggested that the data in Refs. [41,43,44] should be scaled by a factor of 0.85. This recommendation was confirmed in recent photoactivation experiments on $^{92-100}$Mo [5] and ^{144}Sm [46]. In these studies, ^{92}Mo(γ, n) and ^{144}Sm(γ, x) reaction yields ($x = n, p, \alpha$) were also compared with the predictions of TALYS. In accordance with these recommendations, a normalization factor of 0.85 has been applied to the EXFOR data points for all of the nuclei in this study, except for ^{90}Zr, where the data is taken from Ref. [45].

The combination of the three photoabsorption cross section sources listed above (two experimental and one theoretical) define our photoabsorption input, and is henceforth referred to as the experimental photoabsorption cross section (EPACS).

From a conceptual standpoint one should remark that EPACS is a realistic strength function for γ-induced reactions where $E_\gamma \geqslant E^{\min}_{(\gamma,\gamma')}$. Its use in (particle,$\gamma$) reactions relies on the assumption that the strength function does not depend on the energy of the compound nucleus, being the same as for the ground state. The SLO, DLO, and TLO represent parametrizations of the (γ, n) cross sections, and the same remarks as for the EPACS apply. The GLO is constructed for (n, γ) reactions. It includes a modification of the transition strength caused by excitations of the nucleus, which is based on the Fermi liquid theory for a finite temperature. This is the temperature correction term in GLO, which may be considered as an estimate for the possible deviations from the Brink-Axel hypothesis. The temperature correction becomes negligible when the value of E_γ is comparable with $S_n - \Delta$.

D. Input data

To facilitate the comparison between the SLO and GLO strength functions, Eqs. (10) and (11), and those based on the new (γ, γ') data, we have modified the subroutine in the computer code TALYS (Version 1.2) [21] that calculates the

γ-ray strength as a function of energy. Our modification derives the γ-ray strength function using Eq. (9) and

$$T_{\mathrm{E1}}(E_\gamma) + T_{\mathrm{M1}}(E_\gamma) = 2\pi[f_{\mathrm{E1}}(E_\gamma) + f_{\mathrm{M1}}(E_\gamma)]E_\gamma^3, \qquad (18)$$

where σ_γ is the experimental photoabsorption cross section and E_γ is the incident γ-ray energy. Clearly, this is an appropriate way to determine the γ transmission for (γ,particle) reactions. Using it in (particle,γ) reactions implicitly assumes that the Brink-Axel hypothesis is applicable.

The input data containing the experimentally obtained photoabsorption cross sections has been energy binned so as to be consistent with, and thus preserve, the inherent energy grid used for calculations throughout TALYS. Where TALYS required the photoabsorption cross section at energies that did not correspond to a data point, a cubic spline interpolation was performed on the data set to obtain it. Through Eqs. (9) and (18), the strength function and transmission coefficient were calculated.

In the following sections we discuss the reaction cross sections and reaction rates calculated using TALYS. We have performed these calculations using the SLO, GLO, and our EPACS γ-strength functions, as well as the DLO γ-strength function, Eq. (14). Level densities play a sensitive role in the cross section calculations. However because we are motivated by the impact of the γ-ray strength function, we perform all calculations using the TALYS option for the constant temperature (CT) model [47], which corresponds to the default level density option. The width fluctuation correction factor calculation was performed by means of the model [48–50]. The experimental data employed in the next section are for unpolarized reactions (E1 + M1) only. Consequently when using the data in conjunction with a TALYS calculation, care must be taken not to include the M1 contribution twice: once implicitly from the measurement itself and once from the TALYS calculation. To prevent this double inclusion, TALYS calculations were performed with the contribution scaled to zero. To reiterate, M1 was scaled to zero in Eq. (9) only when a calculation was being performed with the unpolarized photoabsorption data as input. For calculations not involving the experimental data, M1 was obtained as outlined in Sec. II B. All other required inputs [such as the optical model potential (OMP) parameters, etc.] were provided by the default options in TALYS.

III. REACTION CROSS SECTIONS

A. $l = 1$ strength functions

The measured and theoretically determined primary photoabsorption cross sections, expressed in terms of the $l = 1$ strength function, are exhibited in Figs. 2 and 3 as a function of γ-ray energy over an energy range of 0–14 MeV (i.e., below the peak of the GDR).

The black symbols refer to the data points from Refs. [14–18] below the neutron threshold, and from Ref. [40] above, the latter renormalized as described in Sec. II D. Pink curves are the DLO E1 strength functions. Black curves on the Mo isotope plots refer to the TLO E1 strength function, given by Eq. (13). Because no deformation was assumed for the nuclei ^{88}Sr, ^{90}Zr, and ^{139}La, black curves on the Sr, Zr, and La isotope plots represent the TLO E1 strength calculations for a single Lorentzian. Error bars for experimental data points are shown on the plots. Typically for energies greater than 7–8 MeV error bars appear very small, owing to the logarithmic scale and partially changing the appearance of the symbols from solid circles to squares. Red points illustrate the strength function at very low energies, in the region where the incident photon populates discrete states. In this region none of the strength function models are appropriate. Red points are not used as input in the calculations.

The EPACS for each nucleus is a composite of the three regions, illustrated for clarity in Figs. 2 and 3. In region I ($0 \leqslant E_\gamma \leqslant E^{\mathrm{min}}_{(\gamma,\gamma')}$) the EPACS is constructed from the TLO parametrization. As discussed above, for the Sr, Zr, and La isotopes no deformation is considered and so the TLO is in these cases coincides with a single Lorentzian. In region II ($E^{\mathrm{min}}_{(\gamma,\gamma')} \leqslant E_\gamma \leqslant S_n$) the EPACS is composed of the experimental data from Refs. [14–18]. Lastly in region III ($S_n < E_\gamma < E_{\mathrm{GDR}} + \Delta$, $\Delta = 8$ MeV) the EPACS is made up of data available in the EXFOR database [40], scaled where appropriate by a factor of 0.85 (see Sec. II D). The EPACS are compared to the E1 strength generated by TALYS, where the thick red and the green curves represent the GLO model [24] and the SLO model [23] respectively. Thin red lines depict the M1 strength, which is smaller than the E1 strength in all of the examples.

Because the GDR parameters used in connection with the SLO and GLO models in TALYS are identical with those in RIPL-2 [19] and correspond to the data in EXFOR [40], the above-mentioned correction factor of 0.85 has been applied to σ_{GDR} in the data files enclosed in TALYS for $^{92-100}$Mo, ^{88}Sr, and ^{139}La. This ensures that rescaled data are compared consistently with rescaled calculations. For the ^{90}Zr case, the σ_{GDR} remained unscaled as explained in Sec. II C.

The region of the GDR is in general well described by both GLO, SLO, and DLO models for all of the nuclei. In the example of ^{92}Mo, the GLO and SLO models slightly underestimate the amplitude of the GDR. This is because the black data points in this region include a contribution from the (γ, np) reaction [43]. The TLO parametrization reproduces the position and amplitude of the GDR in all cases. In all but one case (^{92}Mo) the TLO parametrization predicts a low-energy E1 strength function, which is smaller than that given by both the GLO and SLO models. For this particular example at energies greater than 9 MeV the TLO parametrization agrees much better with the calculations of DLO. In all cases for energies less than about 4 MeV, the DLO results are the smallest, whereas above 12 MeV, they tend to be larger than the other models. Differences between the models and the measured data tend to diminish with increasing energy. To reiterate, the TLO expression has been adopted in the very low E_γ region of the EPACS where experimental data, if available, is only for discrete states. In the majority of cases, the TLO values are within a factor of two of those predicted by the SLO model. The exception is for the triaxial nucleus ^{100}Mo, where the nuclear deformation has a strong impact on the photoresponse function.

Figures 2 and 3 demonstrate that whereas the γ-ray strength function models agree in general with the measured data, there are deviations with respect to the SLO, GLO, DLO, and TLO models at the low-energy tail of the GDR for all of the nuclei. The form of this deviation is an extra strength or a structure in the strength function in the energy range of 6–12 MeV. The cause of the structure in the Mo isotopes remains an open question [51]. The character of the strength function is quite different in the case of ^{139}La, plotted in Fig. 3(b). For $E = 6.5$ MeV ($S_n = 8.78$ MeV) there is approximately a factor of 3–4 increase in the measured strength function, compared to the GLO, SLO, and DLO models. Enhancement of the photoabsorption strength in this region has been interpreted as a pygmy dipole resonance [18]. A similar interpretation has been put forward for strength function enhancement observed in the systems ^{88}Sr and ^{90}Zr, plotted in Figs. 3(c) and 3(d) [16,17]. In the case of ^{90}Zr there is an enhancement of a factor 1.4–1.7, compared to GLO and SLO models, at an energy of 9.5 MeV ($S_n = 11.97$ MeV).

B. A(γ,particle) reaction cross sections

To investigate the sensitivity of statistical model cross section calculations on the strength function and possible GDR low-energy tail strength enhancements, reaction cross section calculations were performed. For each nucleus, the (γ, n), (γ, p), and (γ, α) reaction cross sections were calculated using the EPACS (details explained above). The results were compared to identical calculations performed using photoabsorption cross sections given by the GLO, SLO, and DLO models. Shown in Figs. 4 and 5 are the calculated (γ, n) and (γ, p) and reaction cross sections for the nuclei ^{92}Mo, ^{100}Mo, ^{90}Zr, and ^{139}La. Red curves again refer to the GLO model, green dashed curves to the SLO model, pink dotted curves to the DLO model, and blue dotted curves to the EPACS results (cf. supplemental material for additional nuclei [20]).

Inspection of Fig. 4 shows that strength fluctuations in the absorption cross sections between the neutron-separation energy and about 2 MeV below the GDR peak, visible in the EPACS strength functions plotted in Figs. 2 and 3, show up as fluctuations in the reaction cross section. Of course, fluctuations at energies less than the neutron threshold energy do not influence the calculated (γ, n) cross sections [i.e., there is no enhancement in the ^{90}Zr(γ, n) or ^{139}La(γ, n) cross sections as a result of enhancement below S_n (e.g., at 9.5 MeV or 6.5 MeV)]. A disagreement of a factor of 2–3 is observed between the GLO, SLO, and DLO models near the threshold for ^{100}Mo and ^{139}La, whereas for ^{92}Mo and ^{90}Zr the curves agree fairly well. Again, with the exception of ^{92}Mo, towards the peak of the GDR the differences between the models becomes small, reflecting the convergence of the various strength function models in this region.

In most of the (γ, n) cases, the EPACS reaction cross sections are located between the DLO and GLO models. An exception to this is ^{90}Zr(γ, n) [see Fig. 4(c)]. For ^{92}Mo(γ, n), the EPACS reaction cross section is larger than the other model

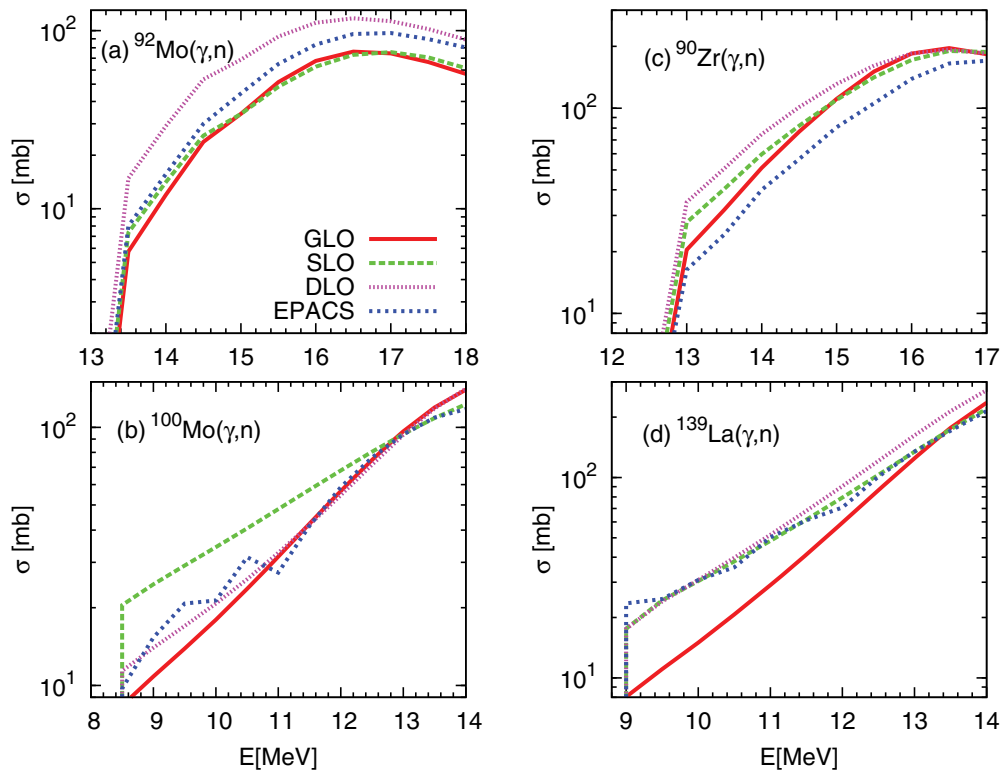

FIG. 4. (Color online) Calculated (γ, n) reaction cross sections for the nuclei ^{92}Mo (a), ^{100}Mo (b), ^{90}Zr (c), ^{139}La (d). Red curves represent reaction cross sections calculated using the GLO model, green dotted curves were calculated using the SLO model, pink dotted curves are from the DLO model, and the blue dashed curves were calculated using our EPACS data (see text for details).

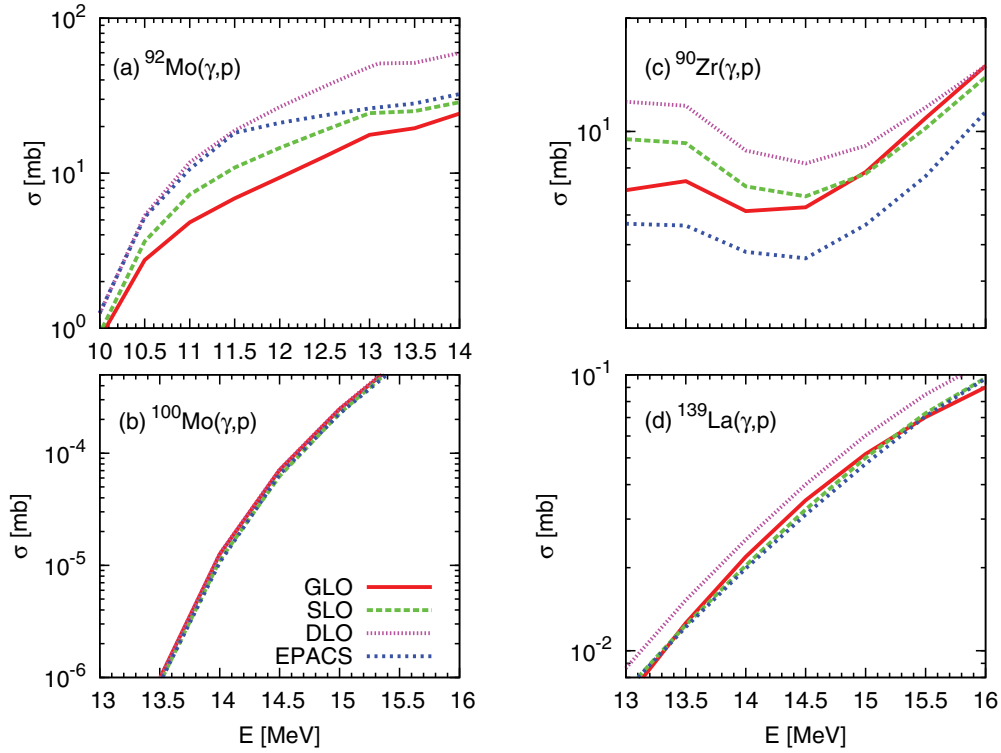

FIG. 5. (Color online) Same as Fig. 4 but for the (γ, p) reaction with target nuclei ^{92}Mo (a), ^{100}Mo (b), ^{90}Zr (c), ^{139}La (d).

predictions (maximum deviation from SLO calculation is a factor of ∼1.4, located at an energy of 16.8 MeV) because the EPACS included a contribution from the (γ, np) reaction [43]. For ^{90}Zr on the other hand, EPACS cross section predictions are smaller than those from SLO, GLO, and DLO (maximum deviation is a factor of ∼0.6, at an energy of 13.0 MeV) because these three strength function models overestimate in this energy region compared to the EPACS data (see Fig. 3).

For the (γ, p) reactions where the proton threshold is lower than the neutron threshold (i.e., for the isotopes ^{92,94}Mo, ^{90}Zr, and ^{139}La), a lower energy region of the strength function is probed. Figure 5 shows that for the (γ, p) reactions there is a reasonably good agreement between the EPACS reaction cross sections and the SLO, GLO, and DLO ones. In most cases the EPACS (γ, p) cross sections follow the other model cross sections very closely, within a factor of 1.5 or better [e.g., $^{96-100}$Mo(γ, p) (cf. supplemental material [20]) and ^{139}La(γ, p)].

A similar agreement exists for the (γ, α) reaction cross sections (cf. supplemental material [20]). As with the (γ, n) calculations, the reaction cross sections calculated from the EPACS lie between the reaction cross sections yielded by the GLO and SLO models. In the case of ^{92}Mo, the factor of 2 enhancement (compared to GLO) in the EPACS at an energy of 11.5 MeV, leads to roughly a factor 2 increase (compared to GLO) in the reaction cross section.

Summarizing this discussion, differences between the γ-strength function models are clearly reflected in the calculated cross sections. The EPACS input generally yields results similar to the traditional SLO and GLO model calculations above the particle thresholds. Where there are differences in the reaction cross section, for instance ^{92}Mo$(\gamma, particle)$B and ^{139}La$(\gamma, particle)$B, it is a reflection of deviations of the EPACS with regard to the SLO and GLO models at energies above the particle thresholds.

C. B(particle,γ)A cross sections

Calculations of (n, γ), (p, γ), and (α, γ) reaction cross sections have been performed in order to test the impact of the EPACS on radiative capture cross sections. Results of the (n, γ) calculations using EPACS and leading to the product nuclei ^{92,100}Mo, ^{90}Zr, and ^{139}La, are shown in Fig. 6 compared to identical calculations performed with the GLO, SLO, and DLO models (cf. supplemental material for additional nuclei [20]).

When the incident neutron energy is low, the average radiative capture width is only from the s wave. Following the prescription of Ref. [52], it is the default setting in TALYS to normalize the γ-ray transmission coefficients to the average radiative capture width at the neutron threshold. In the spirit of investigating the sensitivity of the calculations to strength function model, this default was modified so that the γ-strength function was not scaled, and as such came directly from GDR parameters.

Figure 6 shows that in all cases, the cross section predictions are sensitive to the strength function model choice, with the SLO model producing cross sections between a factor of ∼2.0 and ∼3.5 larger than GLO ones. In virtually all cases, at energies less than 1–2 MeV, both the EPACS and the DLO

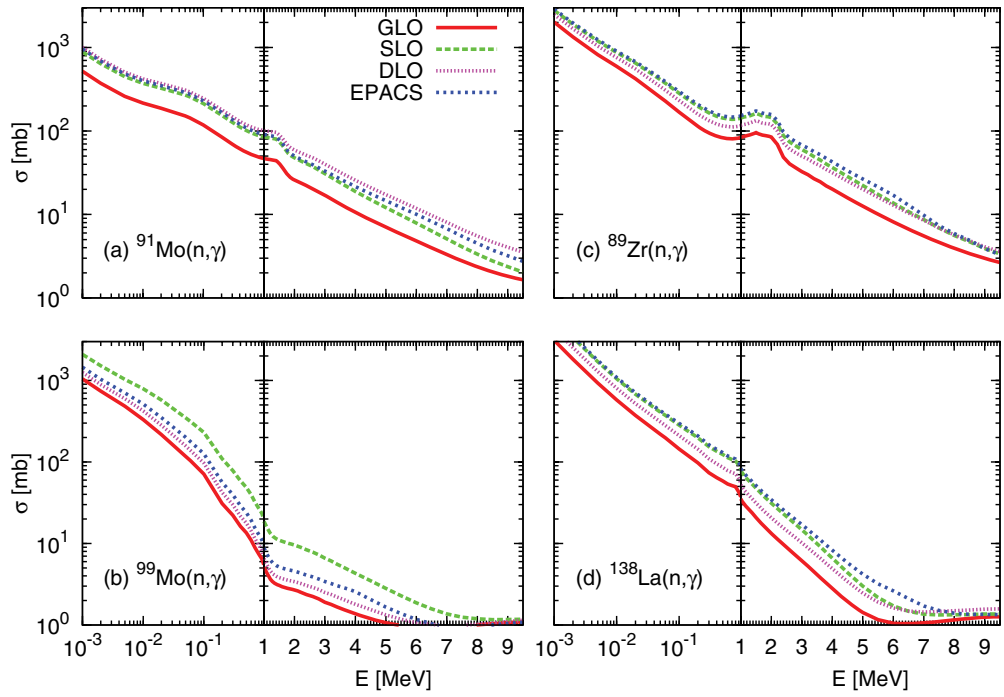

FIG. 6. (Color online) Calculated (n, γ) reaction cross sections for the final state nuclei ^{92}Mo (a), ^{99}Mo (b), ^{90}Zr (c), and ^{139}La (d). Red curves represent reaction cross sections calculated using the GLO model, green dotted curves were calculated using the SLO model, pink dotted lines were obtained with the DLO model, and the blue dashed curves were calculated using our EPACS data (see text for details).

reaction cross sections are between these values, being higher than the GLO ones and lower than the SLO ones. However at energies above 3 MeV, the EPACS predictions for the reactions ^{91}Mo(n, γ), ^{99}Mo(n, γ), and ^{138}La(n, γ) are larger than both SLO and GLO models, corresponding to the fact that for these nuclei the EPACS strength function is larger than the model predictions. This is confirmed by the DLO calculation for ^{91}Mo(n, γ), which is also larger than the SLO and GLO cross sections, in accordance with the larger DLO E1 strength for ^{92}Mo. More specifically, the EPACS La and Zr cross section enhancement comes from the distribution of the extra neutron subthreshold strength. For La, the maximum enhancement is approximately a factor of 1.3 and 2.0, compared to SLO and GLO respectively. The γ-ray strength function is not responsible for the structure feature at about 1–1.5 MeV however, this is generated by the lowest excited state in the (n, n') channel.

In Fig. 7 reaction cross sections calculated with the GLO, SLO and DLO models, and the EPACS input are plotted against experimental data from [53,54] for the reactions ^{95}Mo$(n, \gamma)^{96}$Mo [Fig. 7(b)] and ^{97}Mo$(n, \gamma)^{98}$Mo [Fig. 7(a)]. To evaluate the influence of the level density we compare calculations using the γ-strength models combined with the CT level density [Figs. 7(a) and 7(b)], with identical calculations using the BSFG level density model [Figs. 7(c) and 7(d)].

Compared to the CT, the BSFG cross sections are increased globally by a factor of ∼1.2–2.0. Changes in the relative positions of the models reflect the differences in the energy dependence of the level densities, which are folded with the strength functions. Using the CT level density the experimental ^{95}Mo$(n, \gamma)^{96}$Mo and ^{97}Mo$(n, \gamma)^{98}$Mo data are described very well by the SLO model and reasonably well by the EPACS, being within a factor of 1.7 in the former, and 1.5 in the latter. The GLO cross sections however are a factor of 2.5 lower than the experimental data when combined with CT. For the BSFG level density calculations, EPACS provides the closest description of the data for both ^{95}Mo$(n, \gamma)^{96}$Mo and ^{97}Mo$(n, \gamma)^{98}$Mo, while SLO overshoots the data and GLO, though still lower, is closer to the data for both reactions than it was for the CT calculations. For both reactions, the DLO predictions appear to agree well with the data.

The general tendency of SLO and GLO predictions shown here is similar to the one found in the calculations of Ref. [24], where SLO and GLO calculations were compared with various experimental (n, γ) cross sections. Their HF calculations used the BSFG level density and another level density model (KRK), suggested in Ref. [55]. For the four nuclei considered by Ref. [24], the GLO combined with the BSFG came the closest to the data, whereas they found SLO to be high. For the KRK model, they found the data to be between the predictions of SLO and GLO, as in Figs. 7(c) and 7(d). Using the level density model of Ref. [56], Ref. [39] also found that the GLO model was the most suitable for describing experimental ^{98}Mo(n, γ) data. Though these results appear to be at variance with those presented here, they in fact highlight that other uncertainties in aspects of the HF calculation, such as level densities and width fluctuation corrections, can make it problematic to evaluate which of the considered strength function models provides the best description of

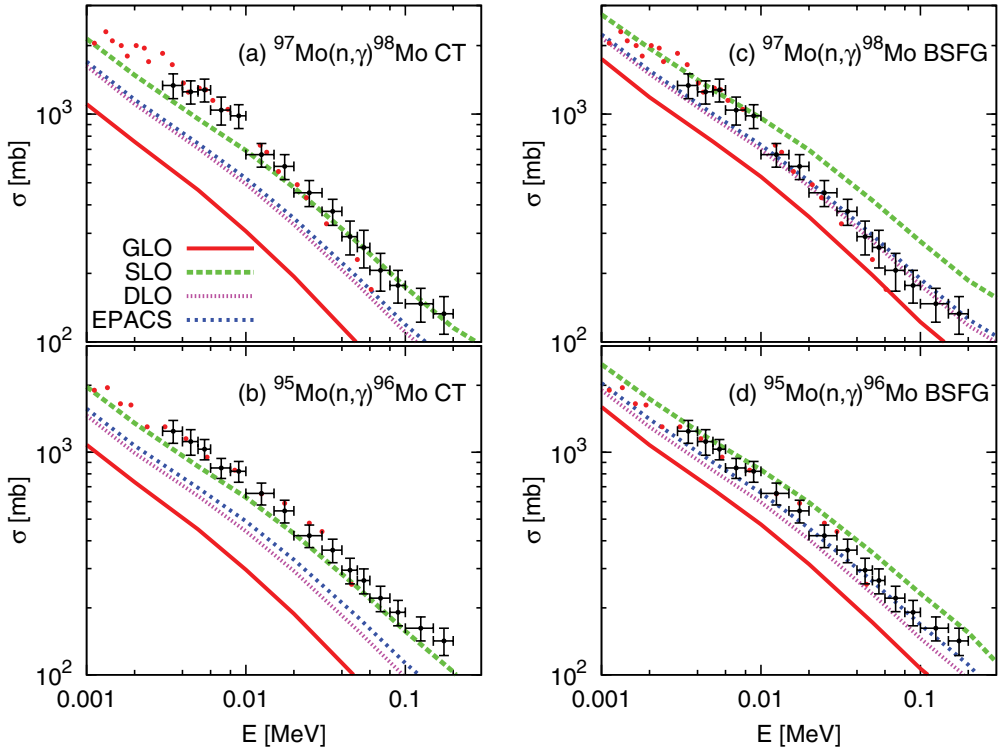

FIG. 7. (Color online) Upper plots: Comparison of the experimental [53] (red dots) [54] (black dots) and calculated ^{97}Mo$(n,\gamma)^{98}$Mo reaction cross section using (left) CT, and (right) BSFG level density models. Red curves represent reaction cross sections calculated using GLO model, green curves were calculated using SLO model, pink curves were calculated with DLO model, and blue curves are calculated from EPACS data. Lower plots: Same as the upper plots, but for ^{95}Mo$(n,\gamma)^{96}$Mo.

experimental (n,γ) cross sections. Comparing Figs. 7(a) and 7(b) with Figs. 7(c) and 7(d) serves as an illustration of the impact of level density model uncertainties on the calculations considered here.

Radiative proton capture reactions on the nuclei ^{91,99}Nb, ^{89}Y, and ^{138}Ba are plotted in Fig. 8, (cf. supplemental material for additional nuclei [20]). These results show similarity to the (n,γ) reactions, discussed above, in that SLO tends to predict higher, and GLO lower cross sections. In general, both the EPACS and the DLO yield results which are very close to those of SLO, with differences not exceeding typically a factor of 1.5, whereas compared to GLO, the deviations can be as much as a factor of 3. Also shown on Fig. 8, where relevant, is the opening of the neutron exit channel. This is responsible for the drop in the ^{138}Ba(p,γ) cross section [Fig. 8(d)] visible at 2.6 MeV.

In Fig. 9 we compare (p,γ) calculations using CT and BSFG level densities [Figs. 9(a) and 9(b) respectively] combined with SLO, GLO, DLO, and EPACS strength functions, with experimental data taken from Ref. [57]. For clarity, Figs. 9(c) and 9(d) show zoomed regions (over an energy region of 1 MeV) of Figs. 9(a) and 9(b).

The overall shape of the data is described well by all of the models, as well as EPACS, for both the BSFG and the CT models. Consistent with the (n,γ) cross sections, the GLO is lower than the SLO. Using the BSFG level density instead of the CT, shifts the GLO closer to the data [cf. Fig. 9(b)]. Up to an energy of 3.7 MeV, agreement between EPACS and the experimental data is excellent in both cases. Above this energy the agreement is not as good, however deviations do not exceed a factor of 2.8 for the CT case and a factor of 3.8 for the BSFG, both occurring at an energy of approximately 4.4 MeV.

The (α,γ) reaction cross sections (cf. supplemental material [20]) again demonstrate that SLO predictions are larger than GLO ones. In most cases EPACS results are between the two models. EPACS yields cross sections marginally larger than SLO for the reactions ^{88}Zr(α,γ) and ^{86}Sr(α,γ), in keeping with the fact that ^{92}Mo and ^{90}Zr have some extra strength in their respective photoabsorption cross sections compared to the SLO and GLO models. The presence of the low-energy resonance in ^{139}La strength function leads to a ^{135}Cs(α,γ) rate which is ∼1.2–2.0 greater than the SLO rate, and ∼1.5–3.5 greater than the GLO rate.

In summary we remark that GLO calculations are in all cases low compared to SLO, DLO, and EPACS. The comparison with experimental (n,γ) and (p,γ) cross sections in this paper and in Refs. [38,58–60] seems to suggest that either EPACS or GLO, combined with the BSFG level density provides the best description of the experimental data. Enhancement features in the strength function [and consequently, if at an energy above particle threshold, in the (γ,n) cross section] are washed out due to the γ cascade. However, enhancement in the strength function (e.g., ^{92}Mo and ^{139}La) does lead to a general enhancement in the various cross sections.

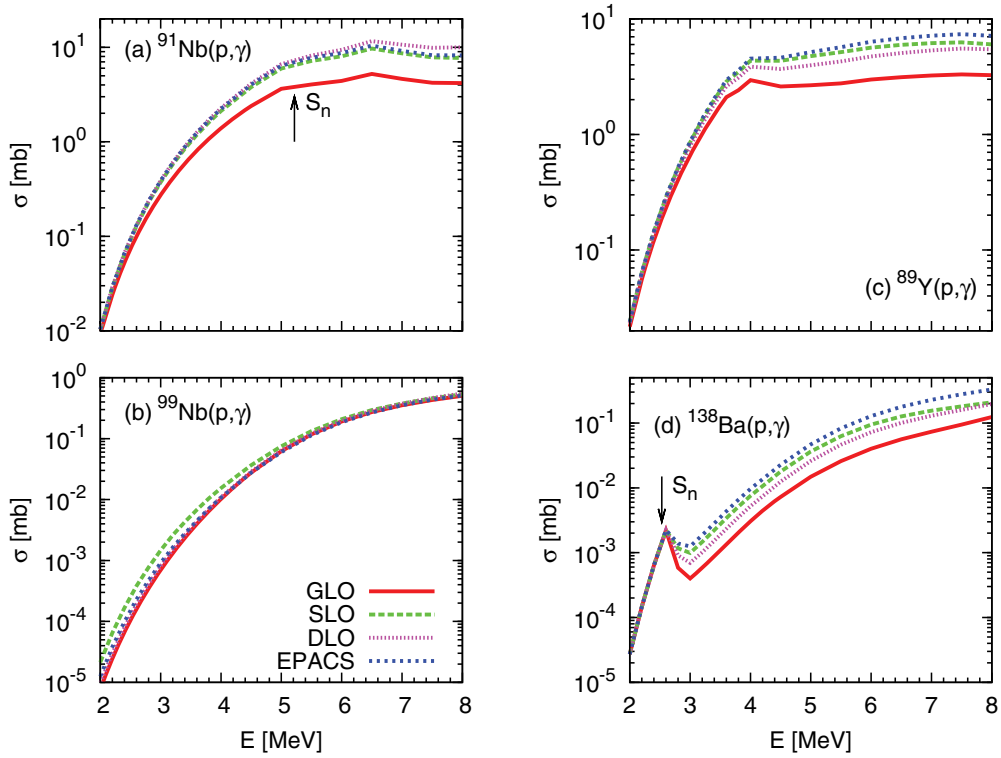

FIG. 8. (Color online) Same as Fig. 6 but for the (p, γ) reaction with final state nuclei ^{92}Mo (a), ^{100}Mo (b), ^{90}Zr (c), and ^{139}La (d).

IV. STELLAR REACTION RATES

A. A(γ,particle)B

Stellar photodissociation reaction rates are calculated in TALYS from the expression

$$\lambda^{*}_{(\gamma,a)}(T) = \frac{\sum_{\mu}(2J^{\mu}+1)\lambda^{\mu}_{(\gamma,a)}(T)\exp\left(-E^{\mu}_{x}/k_{B}T\right)}{\sum_{\mu}(2J^{\mu}+1)\exp\left(-E^{\mu}_{x}/k_{B}T\right)}, \quad (19)$$

where J^{μ} represents the levels of the target nucleus, μ labels the thermally populated state, and E^{μ}_{x} stands for the excitation energy of that state. Photodissociation rates $\lambda^{\mu}_{(\gamma,a)}(T)$ for individual states are found from the integral of a Planck black-body spectrum $n(E_{\gamma}, T)$ (which describes the energy distribution of the stellar γ rays) and the photodissociation cross section

$$\lambda^{\mu}_{(\gamma,a)}(T) = \int_{0}^{\infty} c\, n_{\gamma}(E,T)\sigma^{\mu}_{(\gamma,a)}(E)dE. \quad (20)$$

To understand the potential impact of our EPACS on nuclear astrophysics, stellar (γ, n), (γ, p) and (γ, α) reaction rates were calculated by means of TALYS. The results were compared with identical calculations performed using the SLO, GLO, and DLO models. Results for the (γ, n) reaction rates for ^{92,100}Mo, ^{90}Zr, and ^{139}La are plotted on the left axis of Fig. 10. Plotted on the right axis are the ratios of the reaction rates to the SLO results. The choice of the SLO model as the base is somewhat arbitrary, but is useful because it allows the smaller variations between the models, which are not visible on a log scale, to become apparent. Inspection of Fig. 10 immediately shows that between the SLO and GLO results, the (γ, n) reaction rate is sensitive to within a factor of at most 3 to the choice of strength function model. This sensitivity does not show a strong dependence on temperature, remaining more or less constant. Our EPACS yield (γ, n) reaction rates which either fall between the limits delineated by the GLO and SLO [cf. Fig. 10(b)], or else are enhanced compared to the GLO and SLO predictions [cf. Figs. 10(a), 10(c), and 10(d)]. The enhancement appears to be minor however, a factor of ∼1.1–1.3. (It is stressed that the reaction rate calculations include cross sections with contributions arising from excited states of the target nucleus.)

Displayed in Fig. 11 are the (γ, p) reactions, where once again the ratio of the reaction rates to the SLO reaction rate are shown as thin dot-dashed lines and are plotted on the right axis. The sensitivity of the (γ, p) reactions to the choice of strength model appears to show some temperature dependence for nuclei where the proton separation energy is lower than the neutron separation energy (i.e., ^{92}Mo, ^{90}Zr, and ^{139}La), presumably because the cross sections for these reaction rates have probed a lower region of the photoabsorption cross section. In all cases however SLO predicts larger rates than GLO, by up to a factor of 2. SLO also predicts larger rates than DLO, but the enhancement tends to be very small. As for the (n, γ) calculations, the EPACS results are enhanced compared to SLO and GLO for the nuclei ^{92}Mo, ^{90}Zr, and ^{139}La, though enhancement is relatively minor.

B. B(particle,γ)A

Similar reaction rate calculations have been performed using TALYS for the reactions (n, γ), (p, γ), and (α, γ). Displayed in Fig. 12 are the (n, γ) reaction rates for ^{91,99}Mo,

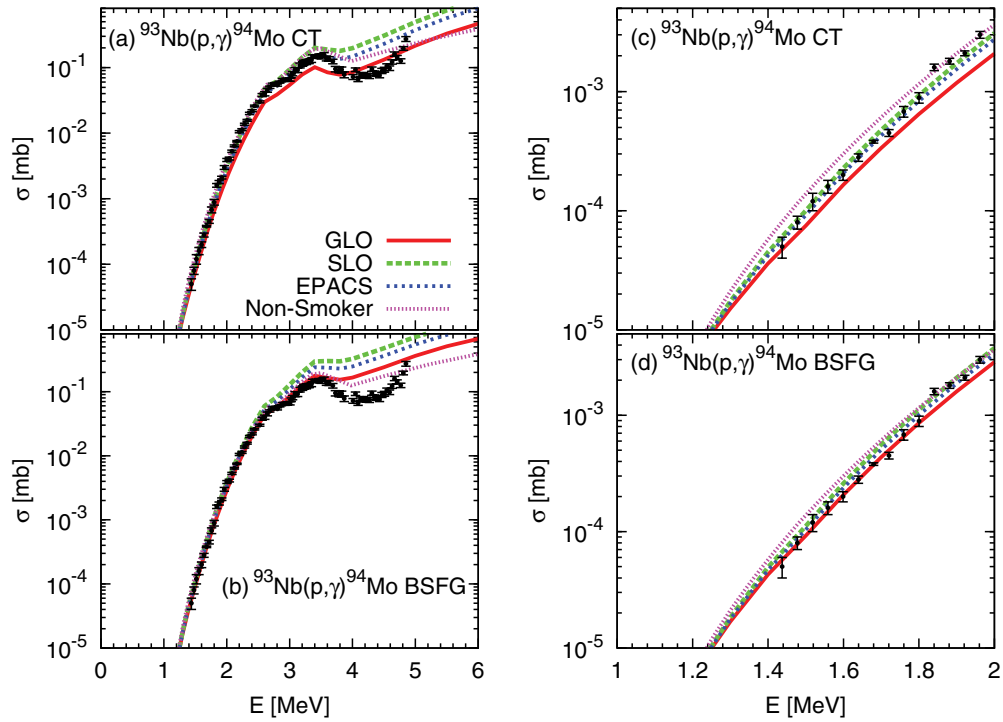

FIG. 9. (Color online) Upper plots: Comparison of experimental data [57] and calculated ^{93}Nb$(p,\gamma)^{94}$Mo reaction cross sections using the CT level density. (Upper right) Zoomed in section highlighting detail. Lower plots: Same as upper plots, but using the BSFG level density model.

^{89}Zr, and ^{138}La. As was the case for the (γ, n) reactions, these rates also show about a factor 3 sensitivity to the strength function model, a factor which does not differ significantly with temperature. For all but ^{99}Mo(n,γ) [Fig. 12(c)] the EPACS predict results that are enhanced compared to the SLO and GLO models. The enhancement is about 7–10% compared to SLO, and 100–150% when compared to GLO results. For the reaction ^{91}Mo(n,γ), the enhancement reflects

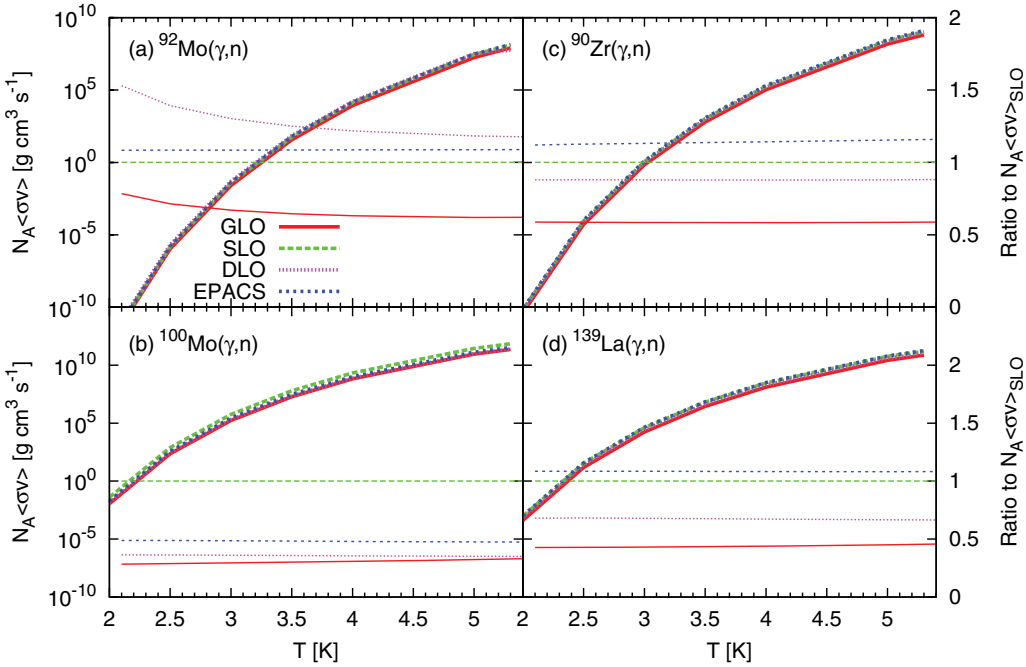

FIG. 10. (Color online) Left axis: Calculated (γ, n) reaction rates plotted on a logarithmic scale as a function of temperature for the target nuclei ^{92}Mo (a), ^{100}Mo (b), ^{90}Zr (c), and ^{139}La (d). Right axis: Reaction rates normalized to SLO, linear scale. Note that 1 corresponds to the same point on both axes.

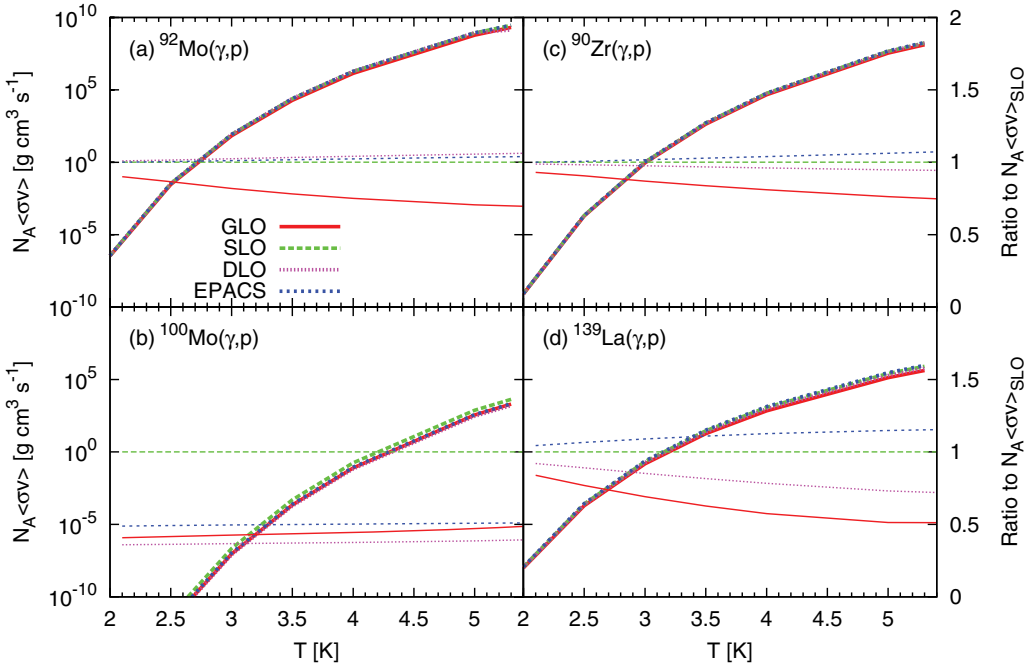

FIG. 11. (Color online) Same as Fig. 10 but for the (γ, p) reaction with target nuclei ^{92}Mo (a), ^{100}Mo (b), ^{90}Zr (c), and ^{139}La (d).

the underprediction of the peak of the γ strength by both the GLO and SLO models [cf. Fig. 2(a)]. DLO also shows an enhancement compared to SLO and GLO due to the same reason. For ^{138}La(n, γ), and ^{89}Zr(n, γ), the EPACS enhancement is due to the extra strength present in the respective experimental strength functions (cf. supplemental material for additional nuclei [20] and details of optical models [61–64]).

As with the γ-induced reactions, it is apparent that the choice of strength function model, SLO or GLO, produces a difference of up to 3 in the (particle,γ) reaction rate, with SLO again predicting the higher values. For the (p, γ) rates, EPACS predicts some enhancement compared to SLO (no more than 5%) for ^{91}Nb, ^{89}Y and ^{138}Ba. These reactions correspond to the nuclei ^{92}Mo, ^{90}Zr, and ^{139}La, and were also found to

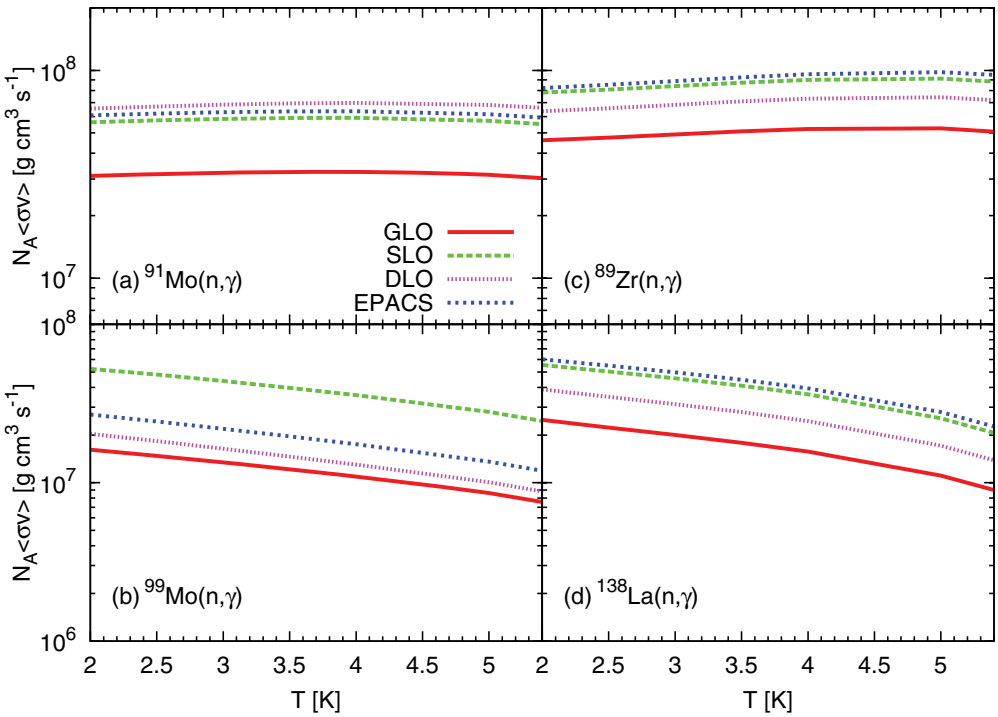

FIG. 12. (Color online) Calculated (n, γ) reaction rates plotted on a logarithmic scale as a function of temperature for the final state nuclei ^{92}Mo (a), ^{100}Mo (b), ^{90}Zr (c), and ^{139}La (d).

be enhanced compared to the SLO and GLO models for the (n,γ) reactions. The EPACS enhancement compared to the SLO and GLO predictions becomes stronger with increasing temperature. This is a consequence of the charged-particle reaction temperature dependence, which comes about due to the Coulomb barrier. Because of this effect, low-energy strength enhancement, present for instance in ^{139}La [Fig. 3(b)], plays a greater role at higher temperatures.

V. DISCUSSION

A major difference between the EPACS strength function and other models is the appearance of resonance-like structures, like the one at 6.5 MeV in ^{139}La [cf. Fig. 3(b)]. Considering (γ,particle) reactions, such structures will only have consequences if they are located above the particle emission threshold. The (γ,n) cross section for ^{98}Mo is an example (cf. supplemental material [20]).

The impact of a resonance-like enhancement of strength below the neutron threshold observed in the (γ,γ') experiments is noticed in the (particle,γ) channels as follows. The primary γ-rays are emitted with a probability that is approximately given by the black-body spectrum $n(E_\gamma, T)$ multiplied by the dipole strength function, where T is the temperature of the compound nucleus. The total cross section is the integral over this distribution. The maximum of the black-body spectrum lies at 2.8 T and its full width at half maximum is 6.3 T, where T is given by Eq. (12). For (n,γ) reactions with thermal neutrons, the temperature is about 0.4 MeV and the strength function is folded with a distribution that has a maximum at $S_n - 1.1$ MeV and a width of 2.5 MeV. With increasing neutron energy the maximum of the black-body spectrum $E_{\max}$ moves to higher energy and its width Δ increases, i.e.,

$$\begin{aligned} E_{\max} &= E + S_n - 2.8T(E+S_n), \\ \Delta &= 6.1T(E+S_n), \\ T(E+S_n) &\approx \sqrt{(E+S_n)8/100}. \end{aligned} \tag{21}$$

Hence, most of the possible resonances in the strength function will be washed out and not show up as a bump in the cross section. If they appear on top of a smooth strength function, such as SLO, they will somewhat increase the cross section over a wide region. Only very strong resonances may generate a shallow bump centered at $E = E_{\rm res} - S_n + 2.8T$, where $E_{\rm res}$ is the energy of the resonance in the strength function. For the charged-particle reactions, the situation is analogous.

The pygmy resonance in the strength function of ^{139}La causes an increase of the (n,γ) reaction cross section by a factor of 1.3 to 2.0, relative to the SLO and GLO models, respectively. However the peak structure seen in the EPACS strength function is actually washed out in the (particle,γ) cross sections. For the case of ^{92}Mo, the low SLO and GLO strength functions compared to the EPACS (and DLO) in the energy region between 8–13 MeV result in an enhancement of the EPACS (and DLO) (γ,n), (γ,p), (γ,α), and inverse reaction cross sections. For other cases, such as (γ,n) reactions on ^{96}Mo and ^{98}Mo, we find no significant difference between EPACS, SLO, and GLO that may be attributed to structures in the strength function below the neutron threshold, plotted in Figs. 2 and 3. This is not surprising because the low-energy EPACS points fluctuate around SLO and GLO values. The above holds true also for the charged-particle induced reaction cross sections. Although they are strongly suppressed by the Coulomb wall, the ratios between the EPACS, SLO, and GLO are similar to those of the neutron-capture reactions. In particular, resonances in the γ-strength function are washed out. As a new feature, the relatively low γ-emission probability (as compared to the one for neutrons) generates irregularities in the cross section, which are caused by the neutron emission.

For the stellar reaction rates, the ratios between EPACS and the other models are nearly constant. This can be understood from the relatively small change of the mean impact energy of the neutrons, which ranges between 100 and 300 keV over the temperature range 2–6 GK. Within this energy range the ratios of the (n,γ) cross sections do not change much (cf. Fig. 12 and supplemental material [20]). Although the cross section in the (p,γ) and (α,γ) channels changes strongly over the energy range, the ratio between the models is also approximately constant. As a consequence, the ratio between the models in the stellar reaction rates is also roughly constant.

Addressing the rate changes attributable to the strength function variations, Ref. [3] found that variations in the (n,γ) and (p,γ) rates had almost no effect on the p nuclei abundances. Comparing just the reaction rates calculated with the TALYS code (Figs. 10–12) we find that SLO produces reaction rates 3 times greater than GLO, and that EPACS predicts rates enhanced by a minor amount compared to SLO. It is therefore unlikely that the reaction rates calculated from our EPACS would significantly impact the abundances of the p nuclei, even owing to presence of low-energy strength enhancement. More critical to the p nuclei abundances are the (γ,p) reactions, and the reaction ^{92}Mo$(\gamma,p)^{91}$Nb has been identified as key importance [3]. For the (γ,p) channel we find agreement between the reaction rates calculated with SLO, GLO, and EPACS to be within a factor of 1.5 for ^{92}Mo, 2 for ^{100}Mo, 1.3 for ^{90}Zr, and 2.5 for ^{139}La, where we also remark that EPACS is enhanced compared to both SLO and GLO. However it seems unlikely that there would be a significant p process impact from these values.

VI. CONCLUSION

By combining new (γ,γ') cross section data with existing (γ,n) cross sections and a three-Lorentzian parametrization, total input photoabsorption cross sections (called EPACS) have been produced for the isotopes ^{92,94,96,98,100}Mo, ^{88}Sr, ^{90}Zr, and ^{139}La. Using these EPACS inputs we have analyzed the reactions A(γ,n), A(γ,p), and A(γ,α), as well as the inverse reactions. This has allowed us to directly investigate the impact of features of observed γ-ray strength functions. This is particularly relevant for the isotopes ^{90}Zr and ^{139}La, which show an especially pronounced strength function enhancement with respect to the often used GLO [24], SLO [23], and DLO [27] parametrizations of the strength function.

The calculations not only probed the sensitivity of cross sections and reaction rates to the γ-strength function, but also tested the accuracy of the currently used SLO, GLO, and DLO models. In particular, the impact of the enhancement

of the γ-ray strength functions in the region of the pygmy dipole resonance on (γ,particle) and (particle,γ) cross sections and reaction rates has been evaluated. Besides the nuclear reaction rates in a temperature range relevant for stellar nucleosynthesis, we have presented strength functions with the aim to deliver a more precise data basis for calculations of cross sections of transmutation-relevant reactions, such as neutron capture.

The A(γ,particle) cross sections directly reflect the strength functions, including possible resonance structures above the reaction threshold. In the case of the A(γ, p) and A(γ, α) stellar reaction rates, absorption is restricted to the relatively narrow energy window set by the thermal distribution of the photon bath and the penetration probability of the Coulomb wall. Resonances within this window will dramatically change the rate. For A(γ, n) reactions resonances at the threshold also drastically change the rate. The resonance around 6.5 MeV observed in ^{139}La does not seem to meet these conditions. The calculated rates reflect the overall smooth trends of the various strength functions studied. In most cases GLO strength functions are lower, DLO and SLO ones larger, than the EPACS values. The resulting variations of the reaction cross sections and the stellar rates are within a factor of 2–3. In the case of the capture reactions, A(particle,γ), the large energy spread of the γ cascades wash out possible resonance structures in the strength function. However, pronounced enhancements of the strength as found for ^{139}La do lead to a modest increase of the (n, γ) cross section. The variations of the calculated reaction cross sections and rates caused by the different strength function models were found to be comparable with differences in level density models and fluctuation corrections used in statistical model calculations. The comparison of experimental cross sections for ^{95}Mo(n, γ), ^{97}Mo(n, γ), and ^{93}Nb(p, γ) with the calculated ones reveals the following: EPACS strength functions combined with the BSFG level density model produces cross sections that compare well with experimental ones. GLO and BSFG, which is a commonly used combination, also produce results that compare well with experiment, particularly in view of the additional examples given in Ref. [24]. Combining GLO with the CT model, however, seems to give cross sections that are too low. This may be a more general result. The combination of SLO and the CT works well for the nuclei in this study. However the combination of SLO and the BSFG gives cross sections that are too large, a result that is consistent with additional examples from literature (cf. Ref. [24]).

ACKNOWLEDGMENTS

This work was supported by the German DFG Project No. KA2519/1-1, the US DOE Grant No. DE-FG02-95ER4093, and by the Joint Institute for Nuclear Astrophysics NSF PHY 0822648. Stimulating discussions with E. Grosse, A. R. Junghans, and A. Koning are gratefully acknowledged.

[1] M. Arnould and S. Goriely, Phys. Rep. **384**, 1 (2003).
[2] M. Rayet, M. Arnould, M. Hashimoto, N. Prantzos, and K. Nomoto, Astron. Astrophys. **298**, 517 (1995).
[3] W. Rapp, J. Görres, M. Wiescher, H. Schatz, and F. Käppeler, Astrophys. J. **631**, 474 (2006).
[4] P. Mohr, K. Vogt, M. Babilon, J. Enders, T. Hartmann, C. Hutter, T. Rauscher, S. Volz, and A. Zilges, Phys. Lett. B **488**, 127 (2000).
[5] M. Erhard, A. R. Junghans, C. Nair, R. Schwengner, R. Beyer, J. Klug, K. Kosev, A. Wagner, and E. Grosse, Phys. Rev. C **81**, 034319 (2010).
[6] Gy. Gyürky, G. G. Kiss, Z. Elekes, Zs. Fülöp, E. Somorjai, A. Palumbo, J. Görres, H. Y. Lee, W. Rapp, M. Wiescher, N. Özkan, R. T. Güray, G. Efe, and T. Rauscher, Phys. Rev. C **74**, 025805 (2006).
[7] N. Özkan, G. Efe, R. T. Güray, A. Palumbo, J. Görres, H. Y. Lee, L. O. Lamm, W. Rapp, E. Stech, M. Wiescher, Gy. Gyürky, Zs. Fülöp, and E. Somorjai, Phys. Rev. C **75**, 025801 (2007).
[8] G. A. Bartholomew, E. D. Earle, A. J. Fergusson, J. W. Knowles, and M. A. Lone, Adv. Nucl. Phys. **7**, 229 (1973).
[9] R. Reifarth, E.-I. Esch, A. Alpizar-Vicente, E. M. Bond, T. A. Bredeweg, S. E. Glover, U. Greife, R. Hatarik, R. C. Haight, A. Kronenberg, J. M. O'Donnell, R. S. Rundberg, J. M. Schwantes, J. L. Ullmann, D. J. Vieira, J. B. Wilhelmy, and J. M. Wouters, Nucl. Instrum. Methods Phys. Res., Sect. B **241**, 176 (2005).
[10] European Organization for Nuclear Research n_TOF facility Report, [http://www.cern.ch/n_tof (unpublished)].
[11] M. Flaska, A. Borella, D. Lathouwers, L. C. Mihailescu, W. Mondelaers, A. J. M. Plompen, H. van Dam, and T. H. J. J. van der Hagen, Nucl. Instrum. Methods Phys. Res., Sect. A **531**, 392 (2004).
[12] J. Klug, E. Altstadt, C. Beckert, R. Beyer, H. Freiesleben, V. Galindo, E. Grosse, A. R. Junghans, D. Legrady, B. Naumann, K. Noack, G. Rusev, K. D. Schilling, R. Schlenk, S. Schneider, A. Wagner, and F.-P. Weiss, Nucl. Instrum. Methods Phys. Res., Sect. A **577**, 641 (2007).
[13] R. Schwengner, R. Beyer, F. Dönau, E. Grosse, A. Hartmann, A. R. Junghans, S. Mallion, G. Rusev, K. D. Schilling, W. Schulze, and A. Wagner, Nucl. Instrum. Methods Phys. Res., Sect. A **555**, 211 (2005).
[14] G. Rusev, R. Schwengner, R. Beyer, M. Erhard, E. Grosse, A. R. Junghans, K. Kosev, C. Nair, K. D. Schilling, A. Wagner, F. Dönau, and S. Frauendorf, Phys. Rev. C **79**, 061302(R) (2009).
[15] G. Rusev, R. Schwengner, F. Dönau, M. Erhard, E. Grosse, A. R. Junghans, K. Kosev, K. D. Schilling, A. Wagner, F. Bečvář, and M. Krtička, Phys. Rev. C **77**, 064321 (2008).
[16] R. Schwengner, G. Rusev, N. Benouaret, R. Beyer, M. Erhard, E. Grosse, A. R. Junghans, J. Klug, K. Kosev, L. K. Kostov, C. Nair, N. Nankov, K. D. Schilling, and A. Wagner, Phys. Rev. C **76**, 034321 (2007).
[17] R. Schwengner, G. Rusev, N. Tsoneva, N. Benouaret, R. Beyer, M. Erhard, E. Grosse, A. R. Junghans, J. Klug, K. Kosev, H. Lenske, C. Nair, K. D. Schilling, and A. Wagner, Phys. Rev. C **78**, 064314 (2008).
[18] A. Makinaga, R. Schwengner, G. Rusev, F. Dönau, S. Frauendorf, D. Bemmerer, R. Beyer, P. Crespo, M. Erhard, A. R.

Junghans, J. Klug, K. Kosev, C. Nair, K. D. Schilling, and A. Wagner, Phys. Rev. C **82**, 024314 (2010).
[19] T. Belgya, O. Bersillon, R. Capote, T. Fukahori, G. Zhigang, S. Goriely, M. Herman, A. V. Ignatyuk, S. Kailas, A. Koning, P. Obložinský, V. Plujko, and P. Young, *Handbook for Calculations of Nuclear Reaction Data, RIPL-2*, IAEA-TECDOC-1506 (IAEA, Vienna, 2006) [http://www-nds.iaea.org/RIPL-2/].
[20] See Supplemental Material at http://link.aps.org/supplemental/10.1103/PhysRevC.85.065808 for additional cross section and reaction rate results, which also contain comparisons with the popular NON-SMOKER reaction rates.
[21] A. J. Koning, S. Hilaire, and M. C. Duijvestijn, TALYS-1.2, *Proceedings of the International Conference on Nuclear Data for Science and Technology, Nice, 2007*, edited by O. Bersillion, F. Gunsing, E. Bauge, R. Jacqmin, and S. Leray (EOP Sciences, Nice, 2007), p. 211.
[22] W. Hauser and H. Feshbach, Phys. Rev. **87**, 366 (1952).
[23] D. M. Brink, Nucl. Phys. **4**, 215 (1957); P. Axel, Phys. Rev. **126**, 671 (1962).
[24] J. Kopecky and M. Uhl, Phys. Rev. C **41**, 1941 (1990).
[25] A. R. Junghans, G. Rusev, R. Schwengner, A. Wagner, and E. Grosse, Phys. Lett. B **670**, 200 (2008).
[26] P. Möller, J. R. Nix, W. D. Myers, and W. J. Swiatecki, At. Data Nucl. Data Tables **59**, 185 (1995).
[27] F.-K. Thielemann and M. Arnould, in *Proceedings of the International Conference on Nuclear Data for Science and Technology*, edited by K. Böckhoff (Reidel, Dordrecht, 1983), p. 762.
[28] T. Rauscher and F.-K. Thielemann, in *Stellar Evolution, Stellar Explosions and Galactic Chemical Evolution*, edited by A. Mezzacappa (IOP, Bristol, 1998), p. 519.
[29] [http://nucastro.org/websmoker.html]; (current version: v5.8.1w; 12-Jan-2007: v4.0w); T. Rauscher and F.-K. Thielemann, At. Data Nucl. Data Tables **75**, 1 (2000); **79**, 47 (2001).
[30] W. D. Myers, W. J. Swiatecki, T. Kodama, L. J. El-Jaick, and E. R. Hilf, Phys. Rev. C **15**, 2032 (1977).
[31] E. R. Hilf, H. v. Groote, K. Takahashi, CERN Report 76-13, p. 142 (unpublished).
[32] N. Pietralla, C. Fransen, D. Belic, P. von Brentano, C. Frießner, U. Kneißl, A. Linnemann, A. Nord, H. H. Pitz, T. Otsuka, I. Schneider, V. Werner, and I. Wiedenhöver, Phys. Rev. Lett. **83**, 1303 (1999).
[33] C. Fransen, N. Pietralla, Z. Ammar, D. Bandyopadhyay, N. Boukharouba, P. von Brentano, A. Dewald, J. Gableske, A. Gade, J. Jolie, U. Kneißl, S. R. Lesher, A. F. Lisetskiy, M. T. McEllistrem, M. Merrick, H. H. Pitz, N. Warr, V. Werner, and S. W. Yates, Phys. Rev. C **67**, 024307 (2003).
[34] C. Fransen, N. Pietralla, A. P. Tonchev, M. W. Ahmed, J. Chen, G. Feldman, U. Kneißl, J. Li, V. N. Litvinenko, B. Perdue, I. V. Pinayev, H. H. Pitz, R. Prior, K. Sabourov, M. Spraker, W. Tornow, H. R. Weller, V. Werner, Y. K. Wu, and S. W. Yates, Phys. Rev. C **70**, 044317 (2004).
[35] G. Rusev, R. Schwengner, F. Dönau, S. Frauendorf, L. Käubler, L. K. Kostov, S. Mallion, K. D. Schilling, A. Wagner, E. Grosse, H. von Garrel, U. Kneißl, C. Kohstall, M. Kreutz, H. H. Pitz, M. Scheck, F. Stedile, P. von Brentano, J. Jolie, A. Linnemann, N. Pietralla, and V. Werner, Phys. Rev. Lett. **95**, 062501 (2005).
[36] G. Rusev, R. Schwengner, F. Dönau, M. Erhard, S. Frauendorf, E. Grosse, A. R. Junghans, L. Käubler, K. Kosev, L. K. Kostov, S. Mallion, K. D. Schilling, A. Wagner, H. von Garrel, U. Kneißl, C. Kohstall, M. Kreutz, H. H. Pitz, M. Scheck, F. Stedile, P. von Brentano, C. Fransen, J. Jolie, A. Linnemann, N. Pietralla, and V. Werner, Phys. Rev. C **73**, 044308 (2006).
[37] M. Guttormsen, R. Chankova, U. Agvaanluvsan, E. Algin, L. A. Bernstein, F. Ingebretsen, T. Lönnroth, S. Messelt, G. E. Mitchell, J. Rekstad, A. Schiller, S. Siem, A. C. Sunde, A. Voinov, and S. Ødegård, Phys. Rev. C **71**, 044307 (2005).
[38] M. Krtička, F. Bečvář, I. Tomandl, G. Rusev, U. Agvaanluvsan, and G. E. Mitchell, Phys. Rev. C **77**, 054319 (2008).
[39] A. C. Larsen and S. Goriely, Phys. Rev. C **82**, 014318 (2010).
[40] [http://www-nds.iaea.org/exfor].
[41] A. Leprêtre, H. Beil, R. Bergère, P. Carlos, A. Veyssière, and M. Sugawara, Nucl. Phys. A **175**, 609 (1971).
[42] B. L. Berman, J. T. Caldwell, R. R. Harvey, M. A. Kelly, R. L. Bramblett, and S. C. Fultz, Phys. Rev. **162**, 1098 (1967).
[43] H. Beil, R. Bergère, P. Carlos, A. Leprêtre, A. De Miniac, and A. Veyssière, Nucl. Phys. A **227**, 427 (1974).
[44] H. Beil, R. Bergère, P. Carlos, A. Leprêtre, and A. Veyssière, Nucl. Phys. A **172**, 426 (1971).
[45] B. L. Berman, R. E. Pywell, S. S. Dietrich, M. N. Thompson, K. G. McNeill, and J. W. Jury, Phys. Rev. C **36**, 1286 (1987).
[46] C. Nair, A. R. Junghans, M. Erhard, D. Bemmerer, R. Beyer, E. Grosse, K. Kosev, M. Marta, G. Rusev, K. D. Schilling, R. Schwengner, and A. Wagner, Phys. Rev. C **81**, 055806 (2010).
[47] A. Gilbert and A. G. W. Cameron, Can. J. Phys. **43**, 1446 (1965).
[48] H. M. Hofmann, J. Richert, J. W. Tepel, and H. A. Weidenmüller, Ann. Phys. (NY) **90**, 403 (1975).
[49] J. W. Tepel, H. M. Hofmann, and H. A. Weidenmüller, Phys. Lett. **B49**, 1 (1974).
[50] H. M. Hofmann, T. Mertelmeier, M. Herman, and J. W. Tepel, Z. Phys. A **297**, 153 (1980).
[51] S. Q. Zhang, I. Bentley, S. Brant, F. Dönau, S. Frauendorf, B. Kämpfer, R. Schwengner, and A. Wagner, Phys. Rev. C **80**, 021307(R) (2009).
[52] D. G. Gardner, in *Neutron Radiative Capture, OECD/NEA Series on Neutron Physics and Nuclear Data in Science and Technology*, edited by A. Michaudon *et al.* (Pergamon Press, Oxford, 1984), p. 62.
[53] S. V. Kapchigashev and Yu. P. Popov, Atomic Energy **15**, 808 (1964).
[54] A. R. Del. Musgrove, B. J. Allen, J. W. Boldeman, and R. L. Macklin, Nucl. Phys. A **270**, 108 (1976).
[55] S. K. Kataria, V. S. Ramamurthy, and S. S. Kapoor, Phys. Rev. C **18**, 549 (1978).
[56] S. Goriely, S. Hilaire, and A. J. Koning, Phys. Rev. C **78**, 064307 (2008).
[57] S. Harissopulos, E. Skreti, P. Tsagari, G. Souliotis, P. Demetriou, T. Paradellis, J. W. Hammer, R. Kunz, C. Angulo, S. Goriely, and T. Rauscher, Phys. Rev. C **64**, 055804 (2001).
[58] J. Kopecky, M. Uhl, and R. E. Chrien, Phys. Rev. C **47**, 312 (1993).
[59] S. A. Sheets, U. Agvaanluvsan, J. A. Becker, F. Bečvář, T. A. Bredeweg, R. C. Haight, M. Jandel, M. Krtička, G. E. Mitchell, J. M. O'Donnell, W. Parker, R. Reifarth, R. S. Rundberg, E. I. Sharapov, J. L. Ullmann, D. J. Vieira, J. B. Wilhelmy, J. M. Wouters, and C. Y. Wu, Phys. Rev. C **79**, 024301 (2009).
[60] A. Chyzh, B. Baramsai, J. A. Becker, F. Bečvář, T. A. Bredeweg, A. Couture, D. Dashdorj, R. C. Haight, M. Jandel, J. Kroll, M. Krtička, G. E. Mitchell, J. M. O'Donnell, W. Parker, R. S. Rundberg, J. L. Ullmann, D. J. Vieira, C. L. Walker,

J. B. Wilhelmy, J. M. Wouters, and C. Y. Wu, Phys. Rev. C **84**, 014306 (2011).
[61] A. J. Koning and J. P. Delaroche, Nucl. Phys. A **713**, 231 (2003).
[62] J.-P. Jeukenne, A. Lejeune, and C. Mahaux, Phys. Rev. C **16**, 80 (1977).
[63] A. Lejeune, Phys. Rev. C **21**, 1107 (1980).
[64] L. McFadden and G. R. Satchler, Nucl. Phys. **84**, 177 (1966).
[65] M. Scheck, P. von Brentano, C. Fransen, U. Kneißl, C. Kohstall, A. Linnemann, D. Mücher, N. Pietralla, H. H. Pitz, C. Scholl, F. Stedile, S. Walter, V. Werner, and S. W. Yates, Phys. Rev. C **75**, 044313 (2007).
[66] L. Käubler, H. Schnare, R. Schwengner, H. Prade, F. Dönau, P. von Brentano, J. Eberth, J. Enders, A. Fitzler, C. Fransen, M. Grinberg, R.-D. Herzberg, H. Kaiser, P. von Neumann-Cosel, N. Pietralla, A. Richter, G. Rusev, Ch. Stoyanov, and I. Wiedenhöver, Phys. Rev. C **70**, 064307 (2004).